Chapter 3

Differentiating the (100) surfaces of Cu_2O Nanocrystals from (111) and (110) for Benzylic C_{sp3}-H Bond Oxidation: Oxidations of Diphenyl Methane to Benzophenone and Cumene to Cumene Hydroperoxide under Mild Conditions.

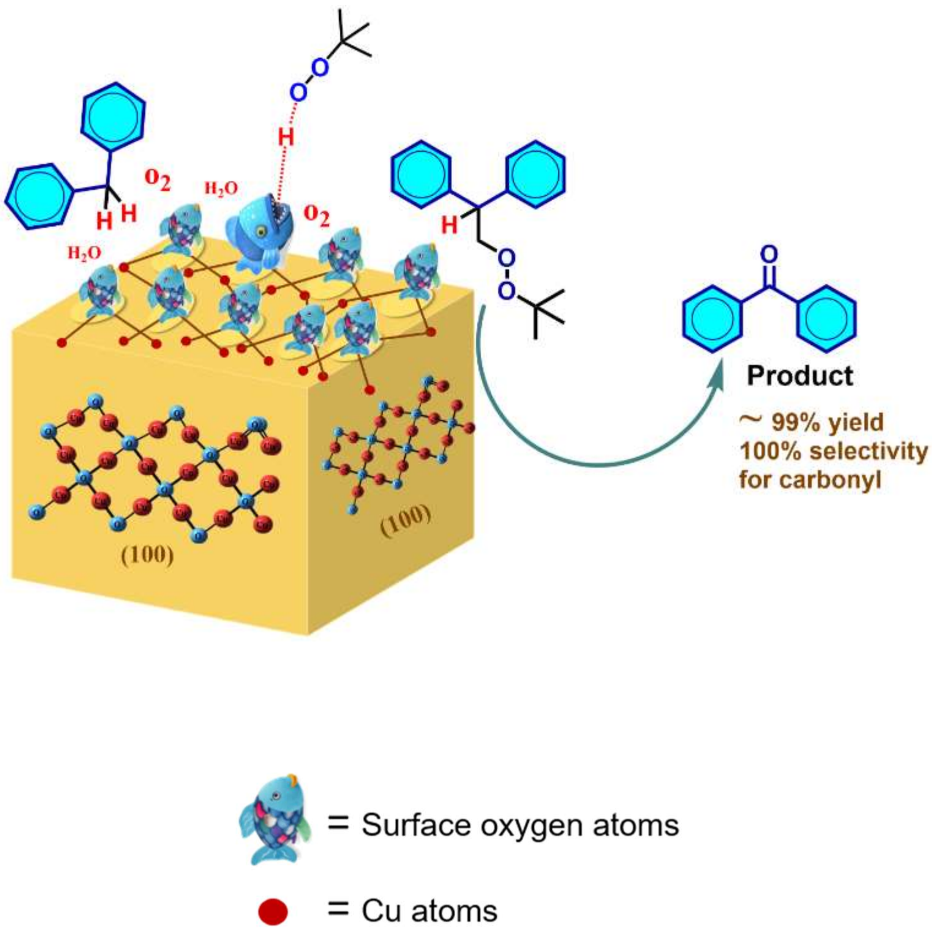

3.1 Introduction

Mankind is always fascinated by shapes since the earlier history of human civilization. Getting inspired by the natural shapes of living or non-living objects they tried to mimic the same by drawing on the canvas of natural caves or in the form of solid constructs. Pictures on the rocky walls, the pyramids of Egypt are some examples of curiosity about the shapes. Nature also prefers the 'shape' to control the biological processes; enzyme catalysis is the best example. However, chemistry point of view, in the field of heterogeneous catalysis, the shape of the catalyst was not given more importance than its particle size and surface area until 2005.[1] It was observed that single-crystalline CeO_2 nanorods having less BET surface area (50.1 m^2g^{-1}) than traditional nanoparticles (62.4 m^2g^{-1}) show better catalytic performance for CO oxidation. This enhanced catalytic activity of CeO_2 nanorods was attributed to the exposed reactive planes {001} and {110}. Physically also, the different facets of the same semiconductor material show different optical, electrical, and photocatalytic properties. For example, Huang's group demonstrated the facet-dependent electrical properties of Cu_2O crystals (Fig. 3.1). They observed {111} facets of Cu_2O octahedra highly conductive, those of {100} of cubic shape moderately conducting while {110} facets of rhombic dodecahedra were non-conducting.[2]They ascribed this conductivity difference due to the presence of a thin surface layer having different degrees of band-bending. Cu_2O crystals of different shapes also exhibit an amazing difference in optical properties in terms of color and band-gap values.

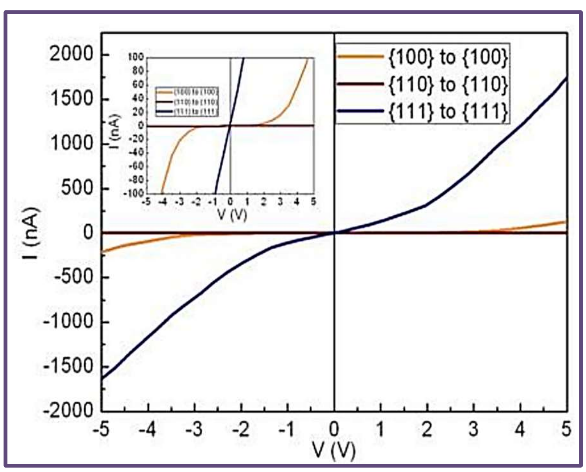

Fig. 3.1 I−V curves for the {100}, {110}, and {111} faces of Cu2O crystals. Inset gives the expanded I−V curves to clearly show the electrical response for the {110} faces. Source; Chih-Shan Tan et.al copyright@ ACS Appl. Mater. Interfaces 2017(Ref).[3]

The drastic difference in the photocatalytic performance of various facets of the same semiconducting material having different shapes is very well reported in a large number of recent literature.[3–7] For example, in the case of Cu_2O, {110} facets of rhombic dodecahedra (*d*-Cu_2O) show the highest photocatalytic activity, while {111} of octahedra (*o*-Cu_2O) moderately active and {100} of cubes (c-Cu_2O) were inactive for the degradation of methyl orange dye.[4,8]In organic transformations, also, the shape-dependent catalytic activity of Cu_2O has been widely studied. For example, M. H. Huang et al evaluated the catalytic efficiency of *c*-Cu_2O, *o*-Cu_2O, and octapod Cu_2O NCs for the synthesis of 1,2,3-triazole by the reaction among various alkynes, organic halides, and NaN_3 under N_2 atmosphere at 55 ºC (Scheme 3.1).

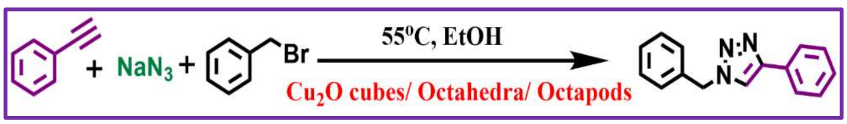

Scheme 3.1 Synthesis of 1,2,3 triazoles

They showed that octahedra bound by {111} facets are the best catalyst to form a 1,4-disubstituted triazole product with a high percent yield (98%) in 2 h.[9] The catalytic activity of Cu_2O NCs having the above morphologies were also reported for the synthesis of 3, 5-disubstituted isoxazoles by regioselective [3+2] cycloaddition (scheme 3.2) [10]. It was demonstrated that *d*-Cu_2O with {110} facets are the most while *c*-Cu_2O with {100} facets are the least catalytically active.

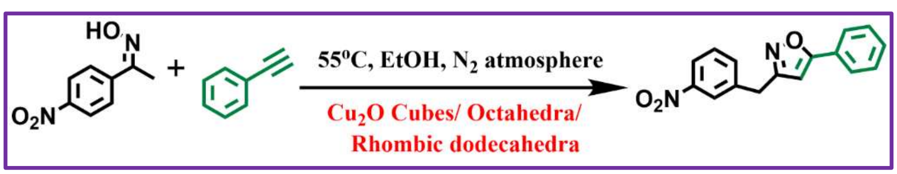

Scheme 3.2 Synthesis of 1,2,3 isoxazoles.

Cu_2O nanoparticles have also been widely used as the catalyst for Ullmann-type coupling reactions for C-N bond formation (scheme 3.3). Commonly, iodobenzene and imidazole are selected as substrates in a modal reaction (three-components click reaction) for screening catalytic efficiency.[11]

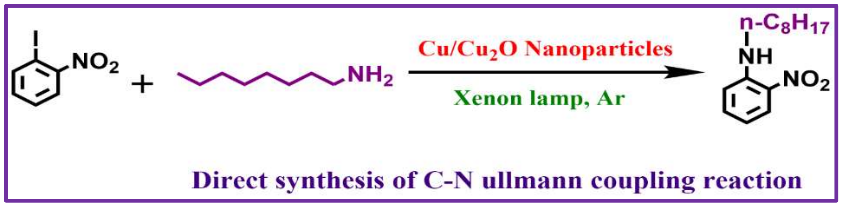

Scheme 3.3 Direct synthesis of C-N Ullmann coupling reaction.

Recently, Li et al. reported (111) faceted Cu/Cu_2O octahedrons and tetrahexahedrons as photocatalysts for C-N Ullmann coupling reaction. They achieved high photocatalytic activity for both aliphatic and cyclic amines reacting with halogenated benzene.[12] From these studies, it can be concluded that Cu_2O nanoparticles with (111) facets exposed having octahedral shapes are suitable for catalytic/photocatalytic organic transformations. Most of these reactions are either coupling or cycloaddition type, but the facet catalyzed organic oxidation processes mediated by free radicals are rarely reported. The question arises in mind, whether these facets exhibit a similar trend of reactivity towards the free radical-mediated oxidation processes? The origin of chemical reactivity demonstrated by a given facet for a particular organic transformation is not explored in-depth as compared to differentiation in their physical properties.

Industrial point of view, oxidation of benzylic sp^3 C-H bond to alcohol or ketone is a very important organic transformation, as it finds applications during the synthesis of pharmaceuticals and fine chemicals.[13] However, the benzylic sp^3 C-H bond is inactive and its functionalization requires transition metal-mediated catalysis, high temperature, and pressure, or the addition of some additives during the reaction. For example, conversion of p-xylene to terephthalic acid, synthesis of cumene hydroperoxide (required for the production of phenol),[14] syntheses of natural products (like artemisinin),[15]pharmaceutical intermediates (like Acrivastine),[16]agrochemicals, and some new advanced materials.[17] Sustainability point of view oxidation processes involving molecular oxygen or ROSs in the presence of light at RT in the aqueous medium will be the best. Industrial production of phenol is carried out via the cumene process and CHP is the major intermediate for the same. Hence, looking at the applications of CHP in other diverse areas like pharmaceuticals, synthesis of α-methyl styrene, oxidative desulfurization, etc., its production is very important. At present, CHP is manufactured from cumene at high pressure (0.7 MPa)[18] and temperature (100 - 140℃) with cumyl alcohol as a major by-product. As CHP is very sensitive to acid, base, heat and presence of transition metal ions as impurities, various catalyst systems are developed to improve the conversion of the cumene oxidation process to CHP. For example, Ag nanoparticles, complexes of transition metal ions[19], N-hydroxyphthalimide (NHPI), and its analogs[20,21] were investigated for selective oxidation of cumene to CHP.[22]

In our previous work, we reported octahedral (111) faceted Cu_2O nanocrystals (*o*-Cu_2O NCs) as a catalyst for benzylic sp^3C-H bond oxidation. Diphenylmethane (DPM) was selected as a substrate for the purpose.[23] Reaction parameters like the type and nature of oxidants, solvents, temperature, and reaction time were optimized to achieve maximum yield and selectivity for the benzophenone as the sole product (and not the carbinol). The experimental results proved the activation of the O_2 molecule through the Single Electron Transfer (SET) from the copper ions exposed on the (111) facets of semiconducting *o*-Cu_2O NCs in the presence of light. We observed that model oxidation reaction takes place with more than 90% yield. However, complete catalyst obliteration took place at the end of the reaction. Hence, the development of a highly selective and productive oxidation protocol involving facets mediated catalysis at RT is the need of time. The complete recovery of the catalyst with the exposed facets intact and becoming ready for the next catalytic cycle is a challenge.

In the present study, we have synthesized *c*-Cu_2O, *d*-Cu_2O, and *o*-Cu_2O NCs having (100), (110), (111) facets exposed, respectively, and compared their catalytic activities for the oxidation of benzylic sp^3 C-H bond present in DPM under the optimized reaction parameters. t-Butyl hydroperoxide (TBHP) was used as an oxidant under aerial atmospheric conditions. Interestingly, we observed different catalytic activities demonstrated by the different facets revealing in terms of reaction completion time and % yield. (100) facets of Cu_2O NCs show the highest catalytic activity for sp^3 C-H bond oxidation in contrast to the cycloaddition and click reactions. Based on the results of chemical kinetics, electrochemical analyses, and DFT calculations, a reaction mechanism has been proposed to explain the catalytic cycle. In the end, we have demonstrated the effectiveness of the developed protocol for the oxidation of cumene to CHP with high selectivity under solvent-less conditions.

3.2 synthesis of catalyst

Synthesis of c- and *d*-Cu_2O NCs. Synthesis protocols of *c*-Cu_2O and *d*-Cu_2O NCs were adopted from the literature.[4] However, we scaled up the reaction volumes to 25 times. For this purpose, 223 mL and 173 mL of DI water were taken in two separate RBFs, which were placed in a water bath at 32-34°C. Then 12.5 mL of 0.1M $CuCl_2$ solution and 2.175g SDS were added to each RBF with vigorous stirring. After complete dissolution of SDS, 4.5 mL of 1.0M NaOH solution was introduced, each. The resulting solution turned to light blue, indicating the formation of $Cu(OH)_2$ precipitates. Finally, 10 mL (for Cc) and 60 mL (for Dh) of 0.1M $NH_2OH.HCl$ was quickly injected. The total volume of solution in each RBF becomes, now, 250 mL. The solutions were kept in a water bath for 1 h for the growth of nanocrystals and centrifuged at 5000 rpm for 3 min. The precipitates were washed several times to ensure the removal of any organic impurities two times with DI water and finally 4 times with absolute alcohol. Samples were dried overnight at 50 °C in the vacuum oven.

Synthesis of *o*-Cu_2O NCs.[23] Cupric acetate ($Cu(CH_3COO)_2.H_2O$, 6.0 mmol) and poly(vinyl alcohol) (PVA, 0.12 mmol (in repeating unit)) were dissolved in 50.0 mL of water at 60 °C. First, the light blue color solution was stirred for 1 h. Then, the aqueous solution of NaOH (120 mmol, 4.8 g in 20.0 mL) was added drop-wise under vigorous stirring. The appearance of dark blue color indicates the formation of cupric hydroxide ($Cu(OH)_2$). Then, 20.0 mL of an aqueous solution of ascorbic acid (18.0 mmol) was added quickly to the above suspension under vigorous stirring, and the color of the suspension changes from blue to green and finally to red after 30 min of stirring. The reaction mixture was centrifuged at 6000 rpm for 10 min. The collected product was washed with DI water (five times) and finally with absolute alcohol and dried in a hot-air oven at 60 °C. See the Supporting Information for further photographs and references (Fig.3.2 and 3.3).

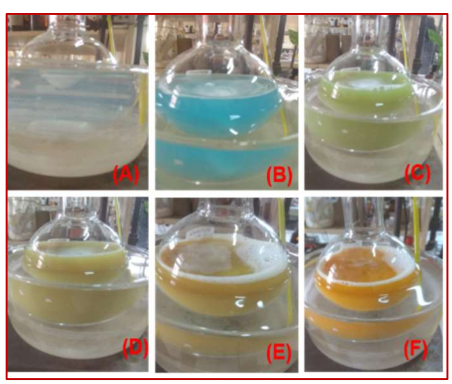

Fig. 3.2 Photographs showing change in the solution color with time during synthesis of Cu_2O nanocubes. (A)Mixture of $CuCl_2$ and SDS (B) Immediately after adding NaOH to the mixture of $CuCl_2$ and SDS aqueous solution, blue $Cu(OH)_2$ formed. (C) after 20s, (D) 30s (E) 40s (F) 60s of addition $NH_2OH.HCl$.

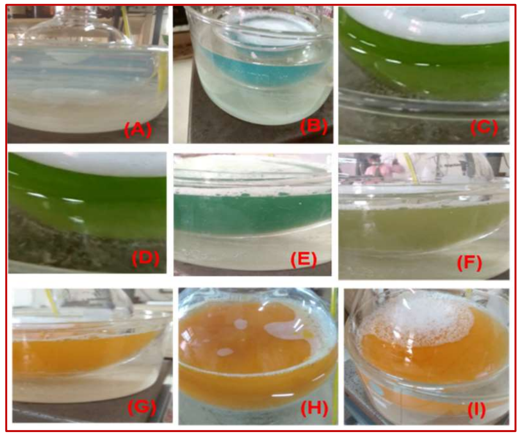

Fig. 3.3 Photographs showing a change in the solution color with time during synthesis of Cu_2O rhombic dodecahedra. (A)The mixture of $CuCl_2$ and SDS (B) Immediately after adding NaOH to the mixture of $CuCl_2$ and SDS aqueous solution, blue $Cu(OH)_2$ formed. (C) after 30s, (D) 40s (E) 60s (F) 8min (G) 10min (H) 20min (I) 60min of addition $NH_2OH.HCl$.

3.3 Characterization.

A powder X-ray diffraction (XRD) pattern was obtained using a PANalytical X-ray diffractometer operated with Cu Kα radiation, λ = 0.15418 nm. The morphology with elemental analysis of the samples was examined by FESEM (JEOL-JSM-7100F). The particle size determination with elemental mapping was carried out by TEM (JEOL-JEM-2100) at 200 kV. The samples were degassed at 80 °C before Brunauer−Emmett−Teller (BET) measurements. The BET surface area was determined by nitrogen adsorption (Micrometrics ASAP 2020) via a multipoint BET method using the adsorption data in the relative pressure (P/P0) range of 0.0-1.0. The desorption isotherm was used to determine the pore size distribution using the Barrett-Joyner-Halenda (BJH) method, assuming a cylindrical pore model. The nitrogen adsorption volume at the relative pressure (P/ P0) of 0.997 was used to determine the pore volume and average pore size. The FTIR (PerkinElmer, Spectrum Two) spectra of the synthesized products were obtained in the range of 400−4000 cm^{-1}. ^{1}H NMR and ^{13}C NMR spectra of the products were recorded on a Bruker Avance 300 MHz spectrometer using TMS as an internal standard in $CDCl_3$. All of the spectra are reported in the Supporting Information. Cyclic voltammetry (CV) and chronocoloumetry were performed using a three electrodes system comprising a platinum wire, glassy carbon electrode, and Ag/AgCl as counter, working, and reference electrodes, respectively. $TBAPF_6$ (tetrabutylammoniumhexafluorophosphate, 0.1M) was used as a supporting electrolyte for this system. The Cu_2O powder-coated GCE electrode (3 mm diameter, 0.07065cm^2) was taken as the working electrode. GCE was thoroughly cleaned by polishing with 0.30 and 0.05mm alumina powder slurries, followed by successive rinsing with ethanol, and then sonicated in DI water for 2 min. The catalyst ink was prepared by mixing 0.2mg freshly prepared NCs of each facet in 500μL absolute alcohol. 3μL of catalyst ink was dropped onto the polished GCE surface and was allowed to dry overnight at room temperature. CV was carried out in the potential range of -1.3 to 1.5 V with a scan rate of 50 mVs^{-1} The Mott−Schottky (MS) measurements were carried out in the potential range of 1.0−2.5 V using the aforementioned electrode system in the model reaction mixture under the optimized conditions. The CV and chronocoloumetry measurements were performed using the electrochemical workstation, CHI600c (CHI Instruments, Austin TX). To investigate the conductivity, the electrochemical impedance spectroscopy (EIS) was carried by sweeping a frequency ranging from 1.2 MHz to 0.1 Hz with an amplitude AC signal of 10 mV by using a Solartron 1260 +1287 interface. From the EIS measurements, the conductivity of the samples was calculated by the equation, $\sigma = l/R_b A$ where σ is the conductivity in S cm^{-1}, R_b is the ohmic resistance of the Cu_2O sample, l is the distance between the two SS electrodes, and A is the total area of the pellet.[24] The hydrodynamic size of nanoparticles was calculated using a BIC 90 plus (Brookhaven) equipped with 35.0 mW solid-state lasers operating at 660 nm, and surface charge (ξ- potential) measurement was carried out using an avalanche photodiode detector.

3.4 Results and Discussion

The phase and purity of as-synthesized Cu_2O NCs of three different morphologies were studied by powder X-ray diffraction (Fig.3.4). The diffraction peaks at 2θ values, 29.65°, 36.52°, 42.42°, 61.55°, 73.73°, and 77.61° are indexed to (110), (111), (200), (220), (311) and (222) planes, respectively, confirming the cuprite phase of Cu_2O (JCPDS#77-0199) with a lattice constant of 4.26 Å having body-centered cubic packing of oxygen atoms and copper atoms occupying the half of the tetrahedral sites. It can be observed from the XRD pattern that the (111)/ (200) ratio for the Oh morphology is the highest due to predominantly exposed (111) facets and it is the least in the case of cubic morphology.[25]The crystallite size was calculated by Debye-Scherrer's equation, $D = k\lambda/\beta\cos\theta$, where D is the average crystallite size, k is the particle shape factor, λ is the wavelength of the X-ray (1.54A° for Cu Kα radiation), β is the line broadening at half the maximum intensity (FWHM) peak for the most intense peak, θ is the Bragg's angle for the most intense peak (in degree).[26] The average crystallite size of the synthesized material was found to be 143, 500, and 500 nm for Oh, Cc, and Dh morphologies, respectively.

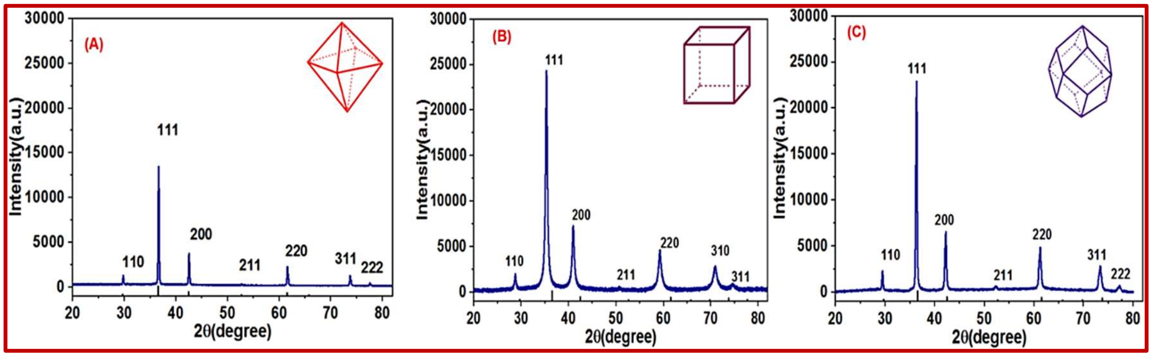

Fig. 3.4 XRD patterns of as-synthesized (a) octahedral (b) cubic (c) dodecahedral Cu_2O NCs.

To further confirm the phase purity and eliminate any probability of the presence of Cu or CuO as impurities in the material, fitting of the experimental XRD data was carried out by employing the Rietveld refinement.[27]Deviation between experimental and theoretical patterns is minimized by the least-squares method. The lattice parameters and unit cell volume were determined from the Rietveld refinement analysis by using the FullProf software (Fig. 3.5). It can be observed from Fig.S1 that the refinement data are in good agreement with the experimental data and the mismatch is negligible. The structural parameters for all synthesized shapes are tabulated in Table 3.1. It is confirmed from the Rietveld refinement that all the three samples of different morphologies are highly phase-pure Cu_2O having space group *Pn-3m* for the FCC lattice. The obtained χ^2 values indicate a good fit with experimental data and the prepared samples are free from any extraneous impurities.

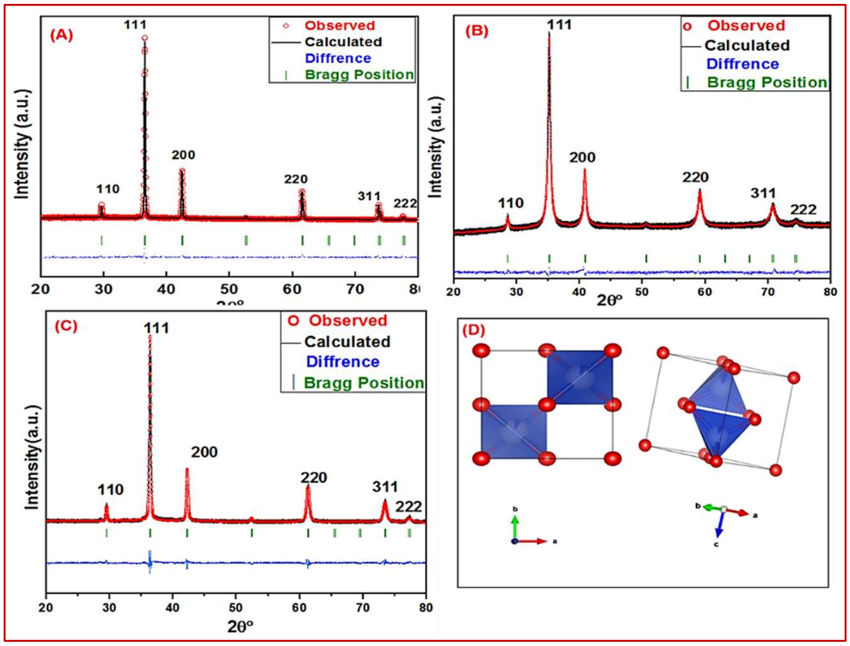

Fig. 3.5 (a-c) Reitveld refined XRD patterns of octahedral, cubic, and dodecahedral Cu_2O NCs and (d) refined structure drawn by using the Vesta software.

Table 3.1 Structural parameters refined through Reitveld refinement analysis.

Structure parameters	Octahedral	Cubic	Dodecahedral
Crystal symmetry	Cubic	Cubic	Cubic
Space group	*P n -3 m*	*P n -3 m*	*P n -3 m*
O1 (x,y,z)	0.0000	0.0000	0.0000
Cu (x,y,z)	0.2500	0.2500	0.2500
u=	0.0289	1.1604	0.7183
v=	-0.0172	-0.3059	-0.2793
w=	0.0257	0.1400	0.0794
Reliability factors(%R)			
Experimental(R_{exp})	13.52	7.26	7.85
Weighted profile(R_{wp})	18.2	10.3	10.9
Bragg intensity(R_B)	3.290	2.422	1.984
Structure factor(R_F)	5.696	2.778	2.317
Goodness of fit(R_{wp}/R_{exp}),χ^2	1.82	1.99	1.94
Density ρ(g/cm^3)	1.584	1.415	1.605
Bond length(A°)			
Cu-O	1.85	1.93	1.85
Lattice parameters(A°)			
a=b=c	4.26	4.33	4.276
Unit cell volume(A^3)	77.385	81.19	78.22

The strain produced in semiconductor crystal lattice during crystal growth processes directly affects its electronic properties and, in turn, its catalytic/photocatalytic activities. Williamson-Hall analysis was employed for estimating crystallite size and lattice strain from the data derived from Reitveld refinement.[28] Strain in particles due to distortions and crystal imperfection was calculated by the equation, $\varepsilon = \beta_{hkl}/4\tan\theta$, assuming the particle size and strain contributions to line broadening are independent of each other. For Williamson-Hall plots, the $\beta\cos\theta$ terms are plotted against $4\sin\theta$. The W-H plot is shown in Fig. 3.6 The crystallite size of all the three morphologies of Cu_2O NCs was calculated from W-H plots (Table 3.2). The positive values of slope indicate the tensile strain (in the case of Cc and Dh NCs) and negative for the shrinkage in the case of Oh NCs. The effective crystallite size is reported in Table 3.2. The slight variation in sizes from those obtained by Debye-Scherrer's formula is due to internal strain. The less values of strain suggest the stability of the exposed surfaces. Hence, it can be claimed that the role of lattice stress and strain on the catalytic activity is negligible and the activities shown by the material are due to its inherent nature.

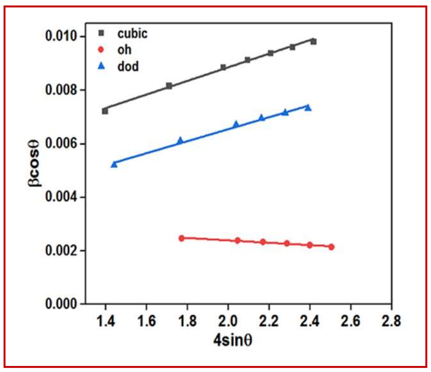

Fig. 3.6 Williamson-Hall plots for synthesized Cu_2O NPs.

Table 3.2 Particle size through PXRD analysis and W-H plot.

Morphology	The average crystallite size (D)by Debye Scherrer's formula (nm)	Effective crystallite size by Williamson-Hall plot (nm)	Strain ($\varepsilon\times10^{-3}$)
Octahedral	4.098682	7.573770492	-0.00237
Cubic	4.1018194	7.248953975	0.01562
Dodecahedral	4.0223389	19.03846154	0.01484

The morphologies of as-synthesized Cu_2O NCs were also studied by FESEM analysis (Fig. 3.7). FESEM images display an almost uniform size distribution. All the eight (111) facets of Oh crystals are depressed from the center of the plane (Fig. 3.7A). While perfect cubes and dodecahedra with narrow size distribution can be observed in Fig. 3.7B and 3.7 C.

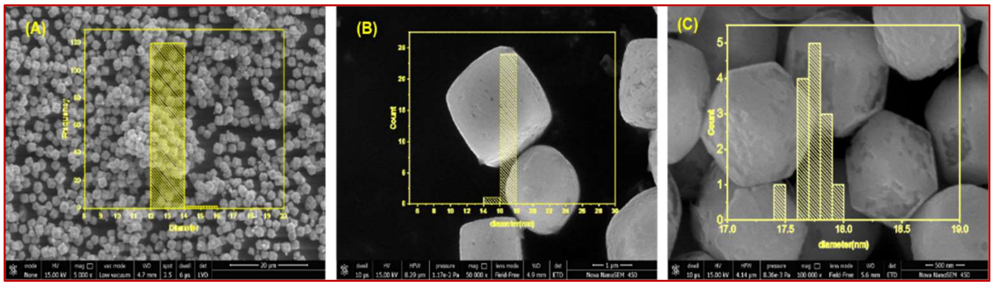

Fig. 3.7 FESEM images of Cu_2O NCs with particle size histograms (A) octahedral (B) cubic and (C) dodecahedral morphologies.

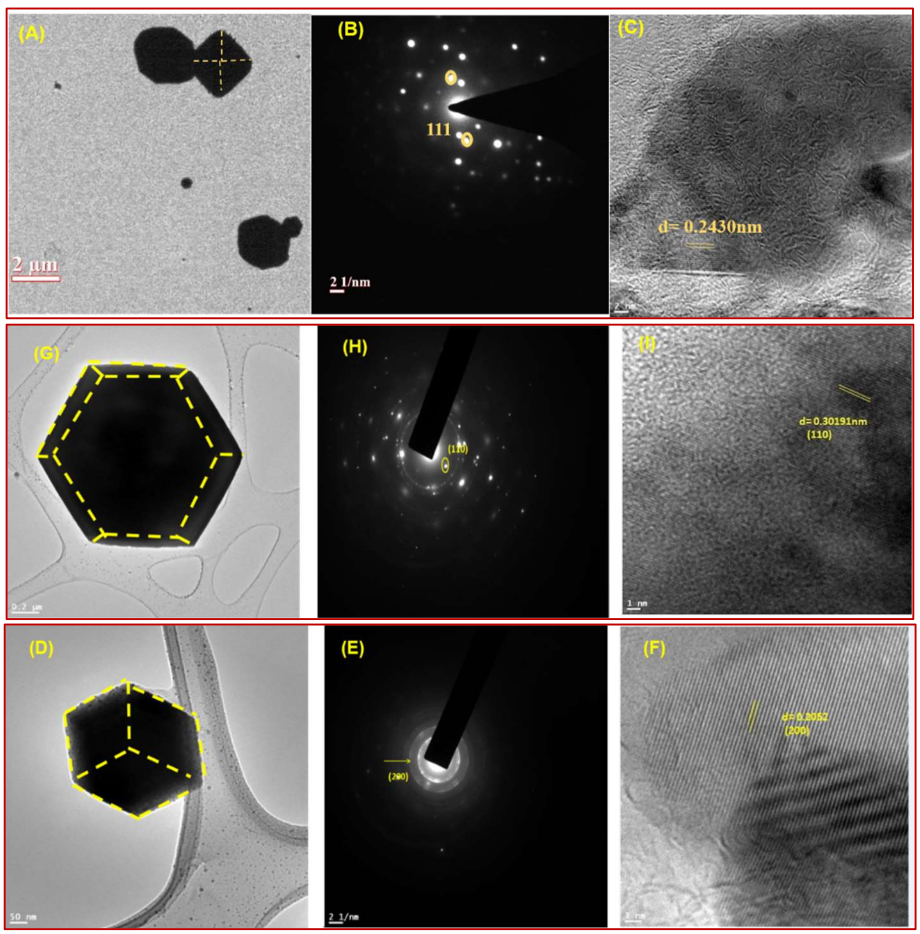

Fig. 3.8 (A) HRTEM image (B) SAED pattern (C) lattice fringes on (111) surface with calculated *d*-spacing of *o*-Cu_2O NCs (D) HRTEM image (E) SAED pattern (F) lattice fringes on (100) surface with calculated d-spacing of as-synthesized *c*-Cu_2O NCs (G) HRTEM image (H) SAED pattern (I) lattice fringes on the (110) surface with calculated d-spacing of as-synthesized *d*-Cu_2O NCs.

The crystallographic features of all the morphologies were studied by using HRTEM and corresponding selected area electron diffraction (SAED) analyses (Fig. 3.8). Figure 9A shows the HRTEM image of *o*-Cu_2O obtained by aligning the electron beam perpendicular to {111} planes. A little truncation of residual {100} planes can be observed in the HRTEM image of oh. The corresponding SAED pattern reveals the highly crystalline nature of the material (Fig. 3.8 B). The HRTEM image shows lattice fringes with a d-spacing of 0.24 nm for (111) planes of cubic phase of *o*-Cu_2O NCs (Fig. 3.8 C). The HRTEM image of the *c*-Cu_2O reveals the single-crystalline nature which is also confirmed by the SAED pattern (Fig. 3.8 D and 3.8 E). The HRTEM image shows lattice fringes with an interplanar spacing of 0.21 nm for (200) planes (Fig. 3.8 F). The HRTEM image of the *d*-Cu_2O reveals the single-crystalline nature of the material which is also confirmed from the SAED pattern (Fig. 9G and 9H). The lattice fringes with a d-spacing of 0.30 nm for exposed (110) planes of *d*-Cu_2O NCs can be observed (Fig. 3.8 I).

The purpose of this study is to evaluate the catalytic activity of the facets of different shapes of Cu_2O NCs, hence, NCs having various shapes were directly synthesized from the methods available in the literature by using various capping agents[4,29]. Once, the targeted morphology was achieved, the crystals were thoroughly washed with deionized water and ethanol three times to ensure the complete removal of the capping agent, this, in turn, nullify the interference of CA during organic transformation. The removal of CA was confirmed from the FTIR spectra (Fig.3.9). The sharp peak at 631 cm^{-1} is due to Cu(I)-O vibrations[30]. The broad V-shaped hump at 3500 cm^{-1} is due to the surface adsorbed water.

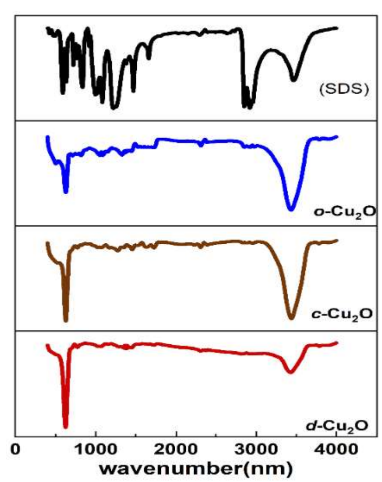

Fig. 3.9 FTIR spectra for synthesized NPs.

Generally, the catalytic activity can be controlled by modifying the surface area of the catalyst. However, factors like the presence of foreign materials (promoters or inhibitors), particle size, morphology and porosity of the particles, electronic structure, defects and surface roughness (like micro kinks, pits, steps, etc), atomic vacancies in the crystal lattice, etc. directly affect the performance of the catalyst. The material exhibiting the catalytic activity for a specific transformation is the collective result of all these parameters. To demonstrate the catalytic activity dominated by certain facets, BET surface area analysis is a useful tool. It can be observed from Table 3.3 that almost no pore voids or space produced due to defects are available. The less value of the surface area is a direct proof of catalysis due to exposed facets.

Table 3.3 BET surface characterization of as- synthesized Cu_2O NCs.

Sr. no	Parameters	Octahedra	Cubic	Dodecahedra
1	SBET(m^2g^{-1})	0.0570	0.0393	2.5273
2	Average pore diameter (A°)	106.89	629.35	343.87
3	Adsorption average pore width (4 V A^{o-1} by BET)(A°)	707.84	243.63	251.68
4	Pore volume(cm^3g^{-1})	0.0000	0.0000	0.0002
5	Total volume in pores(cm^3g^{-1})	0.001 (by DFT)	0.0235 (by DFT)	0.0152
6	Total area in pores(m^2g^{-1})(by DFT)	0.141	0.747	1.261

Benzylic sp^3 C-H bond oxidation of diphenylmethane (DPM, 1) as a model substrate was carried out by t-butyl hydroperoxide (TBHP) as an oxidizing agent in the presence of as-synthesized Cu_2O NCs of various morphologies. We had optimized the reaction parameters for this protocol in our previous study in presence of *o*-Cu_2O NCs as the catalyst[23]. Accordingly,1.0 Equiv. of **1** and 4.0 Equiv. of TBHP were mixed in acetonitrile, in presence of 3.5% (6.0 mg) Cu_2O NCs having different morphologies, and the reaction mixture was stirred at 25ºC-30ºC for 4-6 days over a magnetic stirrer in an aerial atmosphere. Interestingly, when solutions of Cu_2O NCs dispersed in CH_3CN were observed with naked eyes, before the addition of any reactants, a clear differentiation in the color of the solution can be visualized (Fig. 3.10). The progress of the reaction was monitored on the TLC plate using benzophenone (2) and carbinol (CAS No. 91-01-0) as standards. We had also carried out controlled experiments in absence of Cu_2O NCs or TBHP, no product was formed. The results obtained for each morphology of the catalyst are reported in Table 3.4.

Table 3.4 Oxidation of the benzylic sp^3 C-H bond in the presence of Cu_2O NCs of various morphologies.

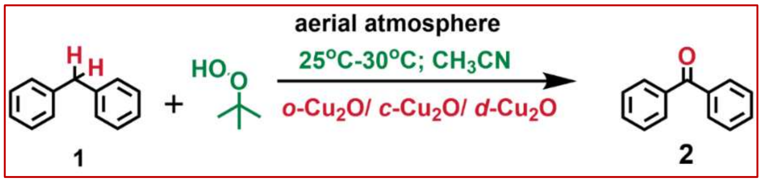

Sr. No.	Morphology	Major surfaces exposed for catalysis	Reaction time (time required to complete the reaction) (days)	Yield [a] (at the end of reaction) (%)	Observations
1	*c*-Cu_2O	{100}	3 (3)	98 (99)	No leaching/obliteration of the catalyst
2	*o*-Cu_2O	{111}	3 (5)	80 (92)	Complete catalyst obliteration
3	*d*-Cu_2O	{110}	3 (4)	88 (92)	Partial catalyst obliteration in the stipulated time period

[an] Isolated yield.

It can be observed from Table.5 that *o*-Cu_2O NCs require 5 days to complete the model oxidation under the optimized parameters resulting in 92% yield. While the *d*-Cu_2O NCs can do the same job within 4 days. It is interesting to note that the *c*-Cu_2O NCs finish the oxidation process with a 98% yield at the end of 3rd day. We observed that complete catalyst annihilation (Cu_2O to CuO) takes place in the case of *o*-Cu_2O, partial for *d*-Cu_2O NCs under an aerial environment while the reaction was completed within 3 days without catalyst annihilation in the presence of *c*-Cu_2O NCs (See photographs in Fig.3.11).

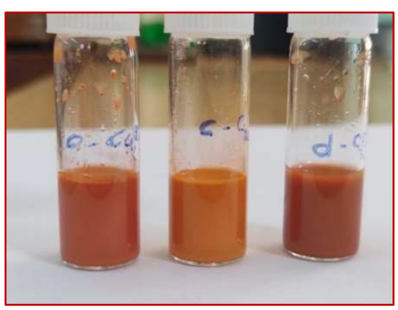

Fig. 3.10 NCs suspension in acetonitrile: *o*-Cu_2O, *c*-Cu_2O, *d*-Cu_2O respectively (left to right)

Exposed facet	When rxn was set	After completion
{111}		
{100}		
{110}		

Fig. 3.11 Appearance of the model reaction mixture at the beginning and at the time of completion of the reaction.

We also carried out further experiments based on our previous work and observations for all the morphologies of Cu_2O NCs. Accordingly, the same model reaction was carried out in the presence and absence of light in an aerial atmosphere. We observed that the (100) surfaces of *c*-Cu_2O NCs become active in the presence of light and can oxidize the benzylic sp^3 C-H bond the carbonyl group very efficiently within 3 days as compared to the other surfaces that emerge from different shapes. To evaluate the rate of reaction, the absorption spectra of the reaction mixture at the end of 24 h were recorded for the model oxidation catalyzed by as-synthesized Cu_2O NCs having different facets exposed. It can be observed from the UV absorption spectra (Fig. 3.12) that the model reaction mediated by *c*-Cu_2O shows the highest absorption intensity at any time due to the presence of the product, benzophenone, followed by *d*-Cu_2O and *o*-Cu_2O NCs. Hence, it can be claimed that the highest catalytic activity was observed for *c*-Cu2O and the least for *o*-Cu_2O NCs in a given time.

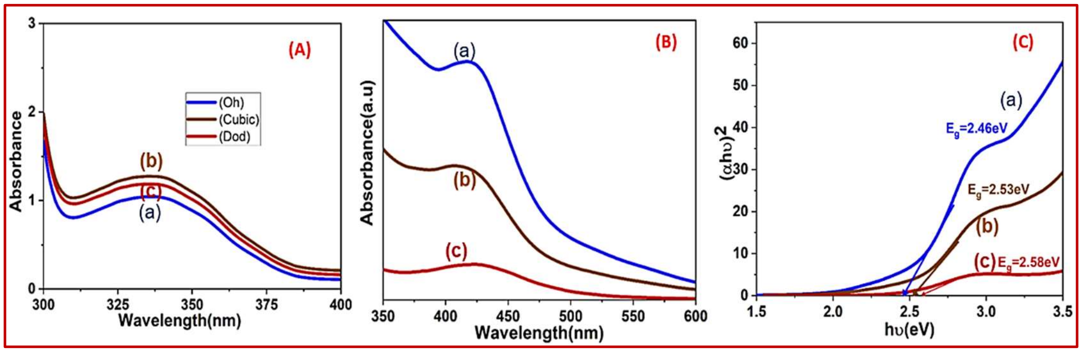

Fig. 3.12 (A) UV absorption spectra of the model reaction mixture at the end of 24 h (B) UV-Visible spectra of (a) *o*-Cu_2O(b) *c*-Cu_2O (c) *d*-Cu_2O in MeCN and (C) corresponding Tauc-plots.

These experimental results contrast the established observations about facets mediated organic transformations. Generally, (111) facets show high activities due to exposed copper ions with the dangling bonds, while (100) surfaces ended with oxygen atoms show the least activities or are inactive.[7,10,31–33] It is logical to think that the high conversion rate may be due to the large surface area offered by catalyst particles at the nano level. The BET surface analysis reveals that the surface area of *d*-Cu_2O is maximum while that of *c*-Cu_2O NCs is minimum (Table 3.3), however, the highest catalytic activity was observed in the second case, confirming the mode of catalysis is due to the exposed surface planes only. To further explore the variation in the reaction rate due to the catalytic activities by various facets, ζ potential measurements of the freshly prepared Cu_2O NCs in pure acetonitrile were conducted in a separate study. The measured ζ potential for *o*-Cu_2O, *d*-Cu_2O, and *c*-Cu_2O NCs are +5.31, +0.58, and -0.58 mV respectively, while the surface charge of Dh is close to neutral whereas that of positive for Oh and negative for Cc which agrees nicely with the crystal plane analysis reported in the literature for Oh, Dh and Cc Cu_2O NCs (Table 3.5)[4].

Kinetic studies of all three sets of reactions under the established condition were carried out to track the reaction pathways. For designing the kinetic study, model experiments in the presence of a catalyst having different morphologies and different concentrations of DPM keeping [TBHP] and [catalyst] constant, were carried out by ignoring the internal and external diffusional effects[34]. For all the concentrations of DPM (1.0, 2.0, 3.0, 4.0 and 5.0 mmol each for 5 days), the concentration of product (benzophenone, absorbs in UV region, $\lambda_{max} = 335$nm) varies accordingly. Hence, from these data, [product] Vs. time was plotted (Fig. 3.13A) (Table 3.6) and the slope of these graphs gives initial rates (Table 3.6). Rate constants were obtained from the slope of the graph $\frac{1}{b-a} ln \frac{a(b-x)}{b(a-x)}$

Vs. time (b > a) (Fig. 3.13B) (Table 3.7). It can be observed that cubic morphology shows the highest value of the rate constant for all the concentration range. Apparent activation energies, calculated for all the facets catalyzed reactions at 303, 313, and 323K by using the Arrhenius equation and slope of the Arrhenius plots, are 80.09, 56.48, and 83.34 kJ/mol for *o*- Cu_2O, *c*- Cu_2O, and *d*- Cu_2O, respectively (Fig. 3.13 C).[35] It is confirmed from the kinetics studies that the overall order of the oxidation process is second-order (Fig. 3.13 B) and it is the first order to [DPM]. Hence, DPM and TBHP both are required to proceed with the reaction. The calculated apparent activation energies for *c*-Cu_2O NCs are much smaller than the reactions mediated by NCs of other morphologies. These results suggest higher catalytic activities at the oxygen-ended *c*-Cu_2O surfaces.

Table 3.5. Hydrodyanamic size and Zeta potential measurements of aqueous solution of Cu_2O NCs.

	DLS	Surface charge	PDI	Hydrodyanamic Diameter(nm)
{111}	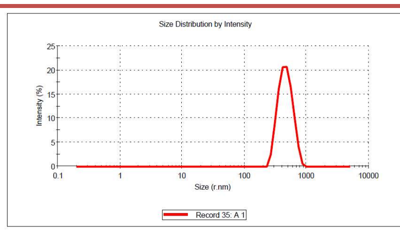	**Zeta Potential** Mobility: 0.41u/s/V/cm Zeta Potentia: 5.31 mv Charge: 0.098 fC Polarity: Positive Conductivity: 11 uS/cm	0.186	421.8
{100}	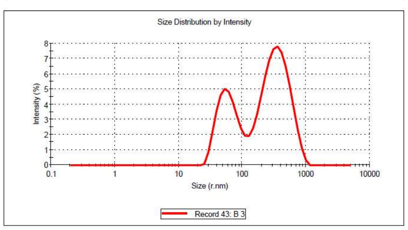	**Zeta Potential** Mobility: -0.04u/s/V/cm Zeta Potentia: -0.58 mv Charge: -0.00377 fC Polarity: Negative Conductivity: 8 uS/cm	0.494	131.4
{110}	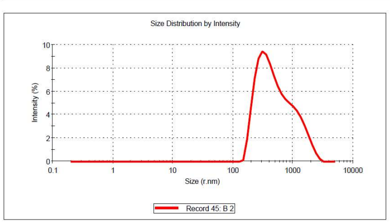	**Zeta Potential** Mobility: 0.04u/s/V/cm Zeta Potentia: 0.58 mv Charge: 0.008 fC Polarity: Positive Conductivity: 8 uS/cm	0.242	423.1

Table 3.6. [product] vs Time (days) plots based on the data from the UV-Vis spectroscopy.

	c-Cu_2O	*d*-Cu_2O	*o*-Cu_2O
1mmol	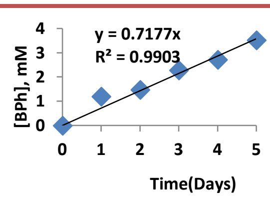	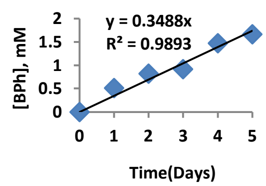	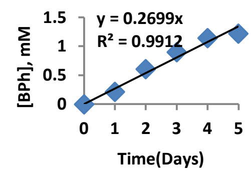
2mmol	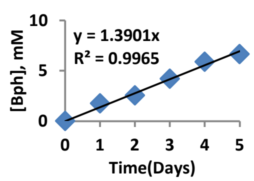	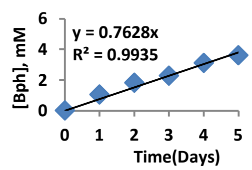	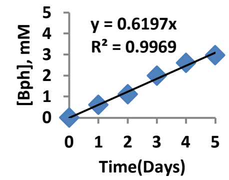
3mmol	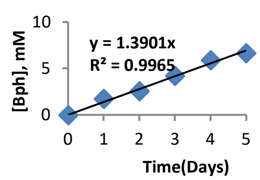	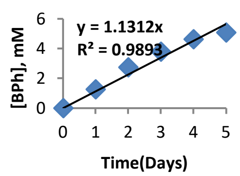	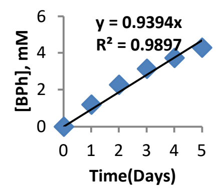
4mmol	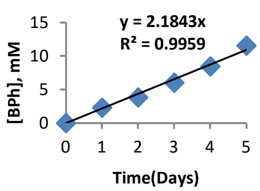	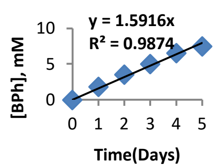	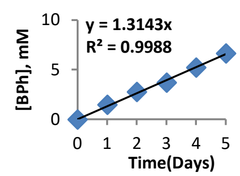

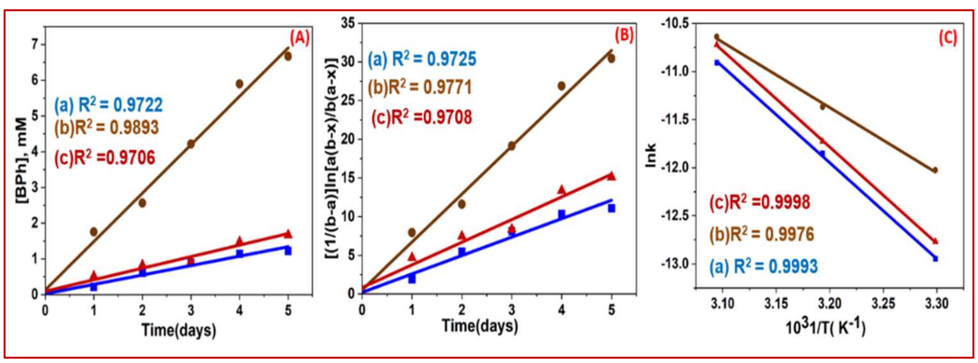

Fig. 3.13. (A) Product [BPh] vs time plots and (B) Rate constant ($mol_{DPM}L^{-1}$ day^{-1}) Vs time plots for 1 mmol DPM (C) Arrhenius plots of octahedral (a), cubic (b), and dodecahedral (c) Cu_2O NCs.

Table 3.7 Calculations of rate constants of a model reaction for each facet.

<table>
<tr><th>[DPM]</th><th>c-Cu₂O*</th><th>d-Cu₂O*</th><th>o-Cu₂O*</th></tr>
<tr><td>1mmol</td><td>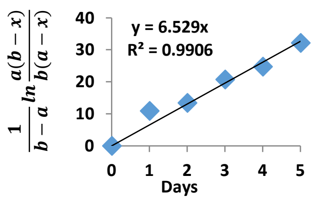
</td><td>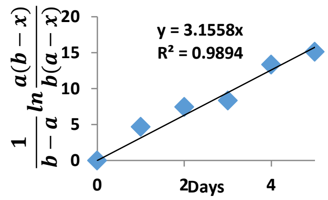
</td><td>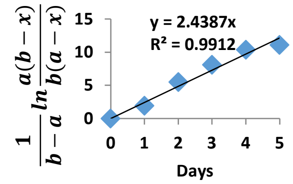
</td></tr>
<tr><td>2mmol</td><td>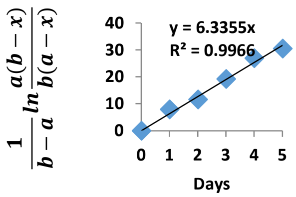
</td><td>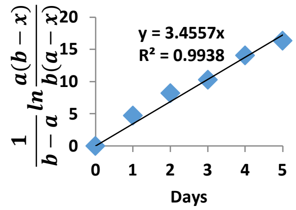
</td><td>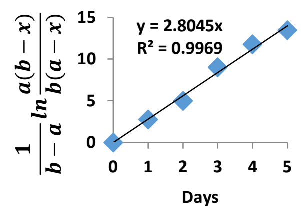
</td></tr>
<tr><td>3mmol</td><td>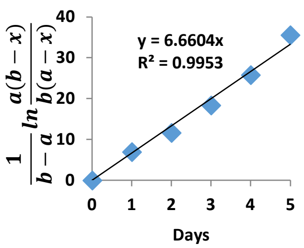
</td><td>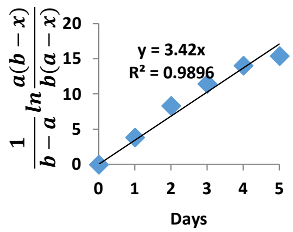
</td><td>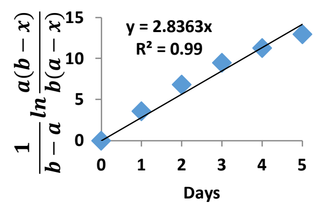
</td></tr>
<tr><td>4mmol</td><td>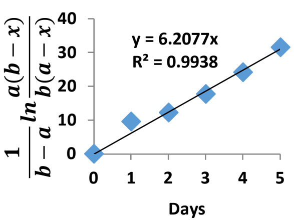
</td><td>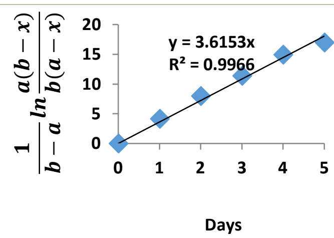
</td><td>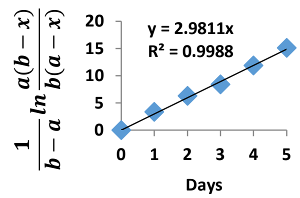
</td></tr>
</table>

To have a deeper idea about the electronic processes taking place on the various surfaces during the model oxidation reaction, electrochemical analyses were carried out. The cyclic voltammograms of Cu_2O NCs of different morphologies coated on a glassy carbon electrode surface, measured at a scan rate of 50 mVs^{-1}, are shown in Fig.3.14 The reversible CV response is obtained for NCs of all the morphologies at a given scan rate proving the suitability of the material for catalytic activities under the given reaction conditions (Fig. 3.14 A). Now, on introducing DPM in the system having Cu_2O NCs coated glassy carbon electrode dipped in acetonitrile, the current density for both the scan rates equally increases (Fig. 3.14 B).

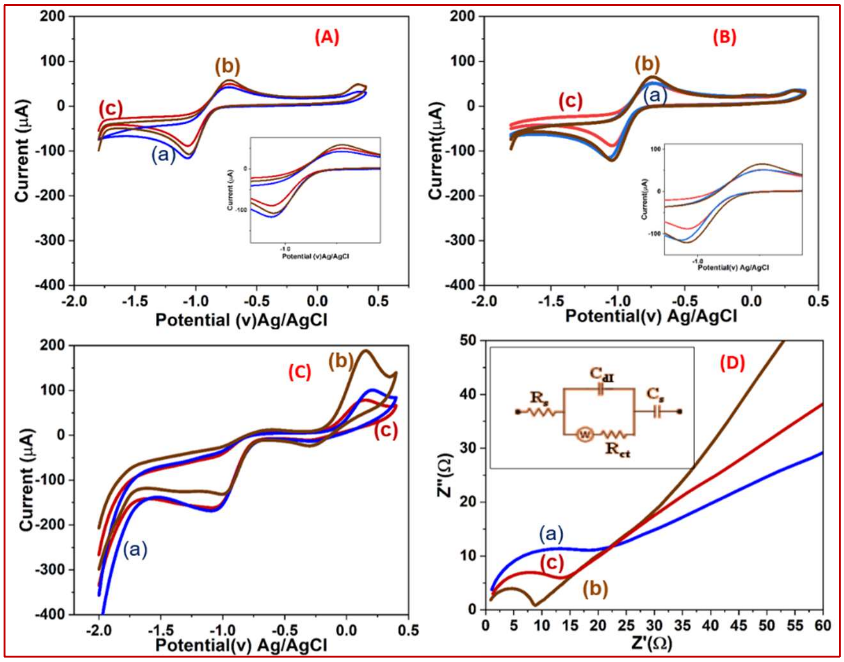

Fig. 3.14 Cyclic voltammograms of (A) Blank Cu_2O NCs coated on glassy carbon electrode dipped in MeCN; inset shows enlarged image for the same (B) on the addition of DPM in above system A (C) on the addition of TBHP in the system B (D) Nyquist plots obtained from impedance measurements (inset; equivalent circuit). [(a) *o*-Cu_2O (b) *c*-Cu_2O (c) *d*-Cu_2O NCs].

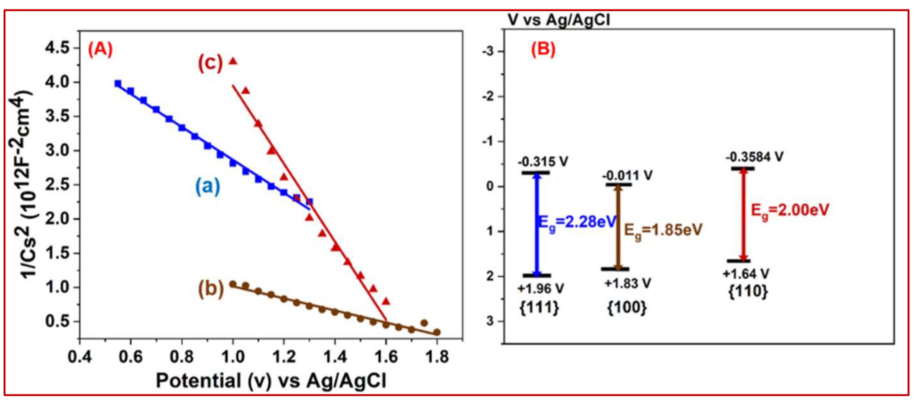

Fig. 3.15 (A) Mott-Schottky plots (B) Flat band potential and bandgap for different planes of Cu_2O NCs. Octahedral (a), cubic (b), and dodecahedral (c).

It is highest in the case of *c*-Cu_2O NCs confirming the adsorption and electronic interaction of DPM with the surface and the absence of any additional redox couples or peaks denying the possibility of other electrochemical processes under prevailing conditions. Interestingly, an additional anodic peak appears with the addition of TBHP in the above reaction mixture (Fig. 3.14 C). However, there is no additional cathodic peak current in the reverse sweep except *c*-Cu_2O NCs. It can be envisaged that with the addition of TBHP, the surface adsorbed DPM irreversibly reacted forming the product, in turn, diffusing out from the electrode surface (EC mechanism),[36] resulting in a decrease in the magnitude of the peak current on the reverse sweep with catalyst annihilation. In the case of *c*-Cu_2O NCs, the anodic current density is the highest substantiates prone oxidation processes (i.e. SET) on the (100) surfaces compared to those of (111) and (110) surfaces with the regeneration of the catalyst surface revealing reversible CV response. Band gaps were calculated (before and after the addition of DPM) from the cyclic voltammetry studies (Table 3.8).

Table 3.8 Band gap calculated from cyclic voltammetry studies.

Exposed facets	**E_g only for catalyst(eV)**	**E_g After introducing of DPM(eV)**
{111}	3.43	3.175
{100}	3.32	2.92
{110}	3.38	2.99

The highest decrease in the band-gap was observed on adsorption of DPM on the (100) surfaces. The charge–transfer kinetics of all samples were studied by impedance measurements, the corresponding Nyquist plots are shown in (Fig. 3.14 D). The charge transfers resistance (R_{CT}) values from the semicircle region are 6.75, 10.4, and 15.2 Ω for *c*-Cu_2O, *d*-Cu_2O, and *o*-Cu_2O, respectively. Hence, it can be said that the charge transfer is easily taking place for cubic NCs during the electrochemical processes, under the given reaction conditions and solvent system.[37,38]The carrier density and flat-band potential of as-synthesized Cu_2O NCs were measured within the potential range of 1.0-2.5 V (Fig.3.15 A). The negative slopes for all the morphologies confirm the p-type semiconductor behavior. The acceptor density is calculated by using the equation ($N_A = 2/e\varepsilon\varepsilon_0 \times$ (slope), where e, ε, ε_0, and N_A are the electron charge (1.602×10^{-19} C), dielectric constant (7.60 for Cu_2O), the permittivity of the vacuum (8.85×10^{-14} F cm^{-1}), and acceptor density (hole density in p-type Cu_2O), respectively) was highest for Cc morphology (Table S9). This requires more potential bias to achieve the Fermi level from the depletion region. The electrochemically effective surface areas of the bare GCE and *o*-Cu_2O/GCE, *c*-Cu_2O/GCE, *d*-Cu_2O/GCE were investigated and compared by chronocoulometry using 0.1mM ferrocene (the diffusion coefficient D is $2.60*10^{-9}$, in MeCN system) as a standard and $TBAPF_6$ (tetrabutylammoniumhexafluorophosphate, 0.1M) as supporting electrolyte. The plots of charge

(Q) Vs time (t) and Q Vs $t^{1/2}$ are shown in (Fig.3.16 (A) and (B)). The surface areas of the working electrode can be calculated based on the Anson equation:

$$Q = 2nFAcD^{1/2}\pi^{-1/2}t^{1/2} + Q_{dl} + Q_{ads} \qquad (1)$$

where Q_{dl} is the charge of double-layer (which could be eliminated by background subtraction), Q_{ads} Faradic charge, D, a diffusion coefficient, c, the concentration of substrate and A represents the effective surface area of the working electrode. Other symbols have their usual meanings.[39]

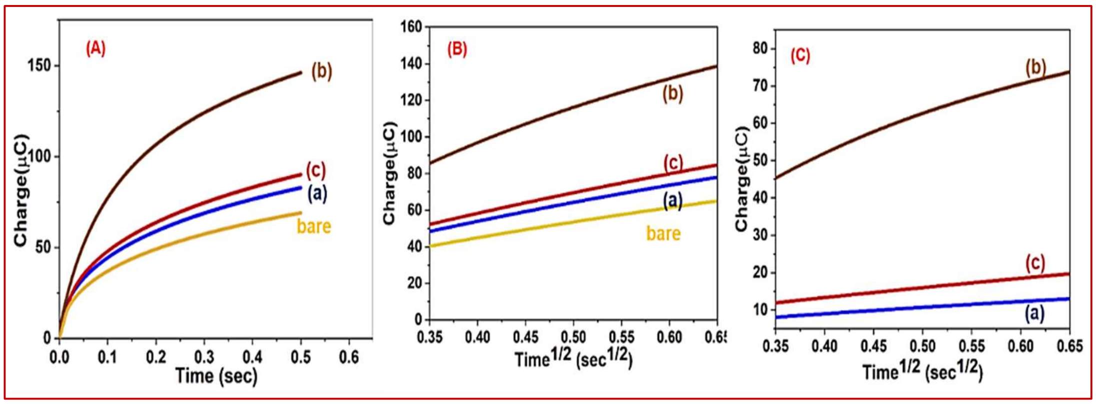

Fig. 3.16 (A) Q Vs t plots of bare GCE (B) corresponding Q-$t^{1/2}$ curves at bare GCE for all facets (C) plot of Q-$t^{1/2}$ derived from chronocoulometric curves for (a) *c*-Cu_2O/GCE (b) *d*-Cu_2O/GCE and (c) *o*-Cu_2O/GCE (background subtracted).

Based on the slopes of the linear relationship between Q-$t^{1/2}$, the effective surface areas (A) of the working electrode were calculated. The results showed (Table 3.9, entry1) that the effective surface area of modified electrodes was increased and observed highest in the case of *c*-Cu_2O. The adsorption capacity Γ_s^- (Table 3.9, entry 7) of *o*-Cu_2O/GCE, *d*-Cu_2O/GCE, and *c*-Cu_2O/GCE NCs was also calculated according to the equation of $Q_{ads} = nFA\,\Gamma^-_s$ by chronocoulometry after point-by-point background subtraction (Fig.8 C), showing highest value for *c*-Cu_2O.[40]

Table 3.9 Chronocoulometry parameters.

		Bare GCE	*o*-Cu_2O/GCE	*c*-Cu_2O/GCE	*d*-Cu_2O/GCE
1.	Electrochemical surface area (cm^2)	0.0689	0.473	0.923	0.810
2.	Slope (C $s^{-1/2}$)	38.23	262.34	511.49	449.11
3.	R^2	0.9983	0.9977	0.9984	0.9988
After background subtraction					
4.	Slopes (C $s^{-1/2}$)	-	147.08×10^{-6}	395.1×10^{-6}	346.3×10^{-6}
5.	Intercept (Q_{ads})	-	5.82×10^{-6}	25.25×10^{-6}	16.68×10^{-6}
6.	R^2	-	0.9977	0.9985	0.9995
7.	Adsorption capacity (mol/cm^2)	-	4.10×10^{-7}	6.62×10^{-7}	4.99×10^{-7}

3.5 DFT simulation. Geometric and electronic properties of (111), (110), and, (100) surfaces of Cu_2O NCs.

Firstly, the structural properties of Cu_2O (111), (110), and (100) surfaces were investigated. The surface structure of (110) and (100) can be altered by varying the surface termination. Herein, we focus on the surfaces terminated by Cu and O atoms as they are thermodynamically more favorable under realistic catalytic conditions[41–43]. The top and side views of optimized structures of Cu_2O (111), (110), and (100) surfaces of NCs are shown in Fig.3.17 along with the computed bond parameters and angles.

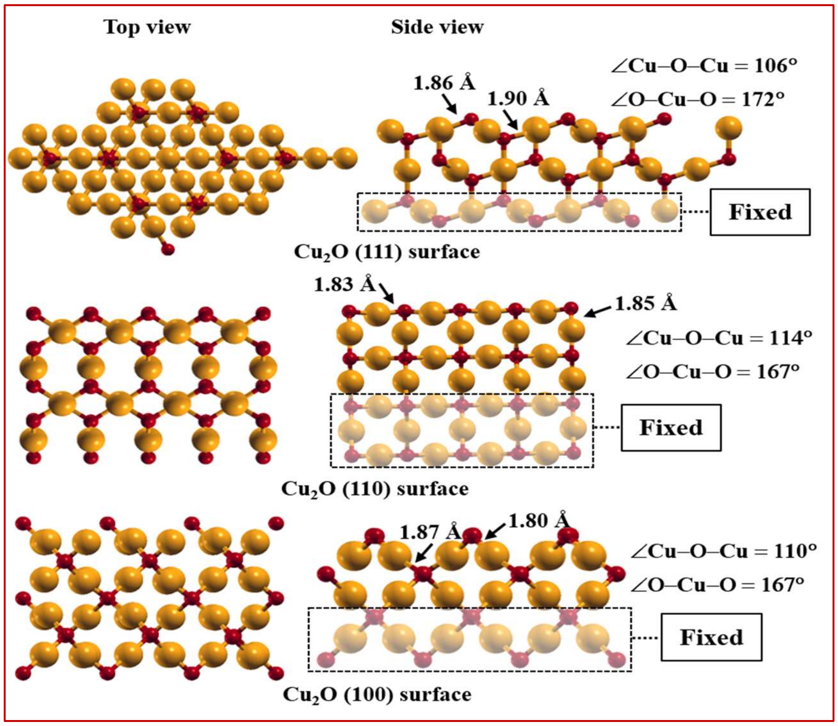

Fig. 3.17 Top and side views of the optimized periodic slab models of Cu_2O (111) (upper panel), Cu_2O (110) (middle panel), and Cu_2O (100) (bottom panel) surface with the structural parameters. Color key: Cu (yellow) and O(red).

The detailed information on computational parameters adopted for the optimization of Cu_2O (111) surface and structural properties are discussed in our previous report. [23]The density of states (DOS) of (111), (100), and (110) surfaces of Cu_2O NCs are shown in Fig. 3.18 (a-c) along with the frontier orbital analysis of the Fermi states in Fig. 3.18(d-f). The band-gap is in the range of 1-1.8 eV, which is required for photocatalytic activity under visible light. Our results on calculated DOS are in agreement with the previous reports[33,41]. For the clear view, only the top-layer atoms were illustrated. It can be seen that the surface oxygen (O) sites are the main contributors to the Fermi state of these surfaces, implying that it is more likely to be the active sites for electron-donating reactions.

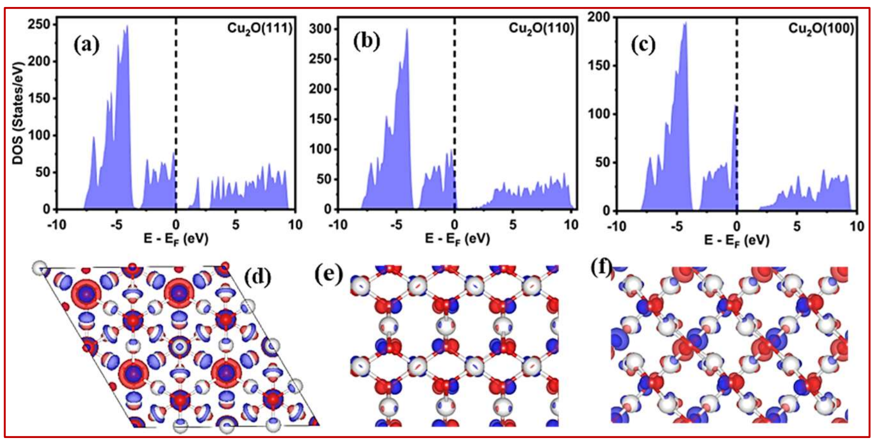

Figure 3.18. The density of states of (a) Cu_2O (111) (b) Cu_2O (100) and (c) Cu_2O (110) surfaces. The charge density plot of Fermi states of (d) Cu_2O (111) (e) Cu_2O (100), and (f) Cu_2O (110) surfaces. The iso-surface value set to ±0.0008 e/Å^3. The blue and red colors represent the depletion and accumulation of charge, respectively. Color key: Cu (white) and O(red).

3.5.1 Adsorption energetics. The oxygen molecule (O_2) and t-butyl hydroperoxide (TBHP) adsorbed on Cu_2O (111),[23] (110), and (100) surfaces are presented in Figure 3.19. For the comparison, the calculated adsorption energy (using Eq. 3, in the experimental section) of O_2 and TBHP over Cu_2O surfaces along with the structural parameters and angles are depicted in Table 3.9 Similar to the Cu_2O (111) surface, O_2 also gets adsorbed in superoxo state over the Cu atom of the (110) surface with the -0.67 eV adsorption energy.

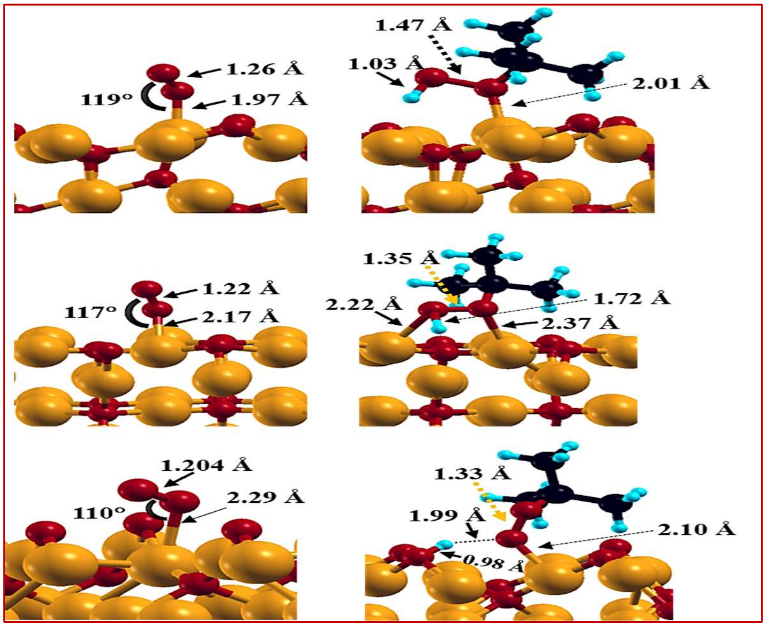

Fig. 3.19 The optimized structure of O_2 and t-butyl hydroperoxide (TBHP) adsorbed Cu_2O (111) (upper panel), Cu_2O (110) (middle panel) and Cu_2O (100) (bottom panel) surfaces with the computed structural parameters. Color key: Cu (yellow), O (red), C (black), and H (cyan).

Table 3.9 The calculated adsorption energy (E_{ads}) of the molecules species over Cu_2O surfaces along with the structural parameters (R_{O-O} and R_{Cu-O}) and angle.

Species	E_{ads} eV	$R_{(O-O)}$ Å	$R_{(Cu-O)}$ Å	∠Cu–O–O
		Cu_2O(111)[a]		
O_2	-1.50	1.26	1.97	119°
TBHP	-1.31	1.47	2.01	-
		Cu_2O(110)		
O_2	-0.67	1.22	2.17	117°
TBHP	-1.69	1.35	2.22, 2.37	-
		Cu_2O(100)		
O_2	-1.14	1.204	2.20	-
TBHP	-2.78	1.33	2.10	-

To investigate the interaction mechanism of the TBHP and DPM molecules with (110) surfaces, different orientations of the molecules were considered. The most favorable configuration of TBHP adsorbed over (110) surface with the computed bond parameters is presented in Figure 3.19. Similar to our previously reported work on (111) surface, the interaction between TBHP and (110) surface mainly arises from the interaction of O atoms of the TBHP molecule and Cu atom of the surface with the adsorption energy of -1.69 eV.

For the (100) surface, different orientations of the adsorbate molecules were considered for the adsorption. The optimized structure of the O_2 and TBHP adsorbed (100) surface is presented in Figure 3.19. In the case of (100) surface, O_2 gets adsorbed in the superoxo state over the Cu atom (second Cu atomic layer) with the -1.14 eV adsorption energy. Interestingly, we observed that the hydrogen atom of the OH bond split from the TBHP molecule and attached it to the oxygen atom of the (100) surface (Figure 3.19). While the rest of the molecule interacts with the surface via the oxygen atom of the molecule with the -2.78 eV interaction energy. Same as (111) surface, DPM molecule physisorbed over the (110) and (100) surfaces.

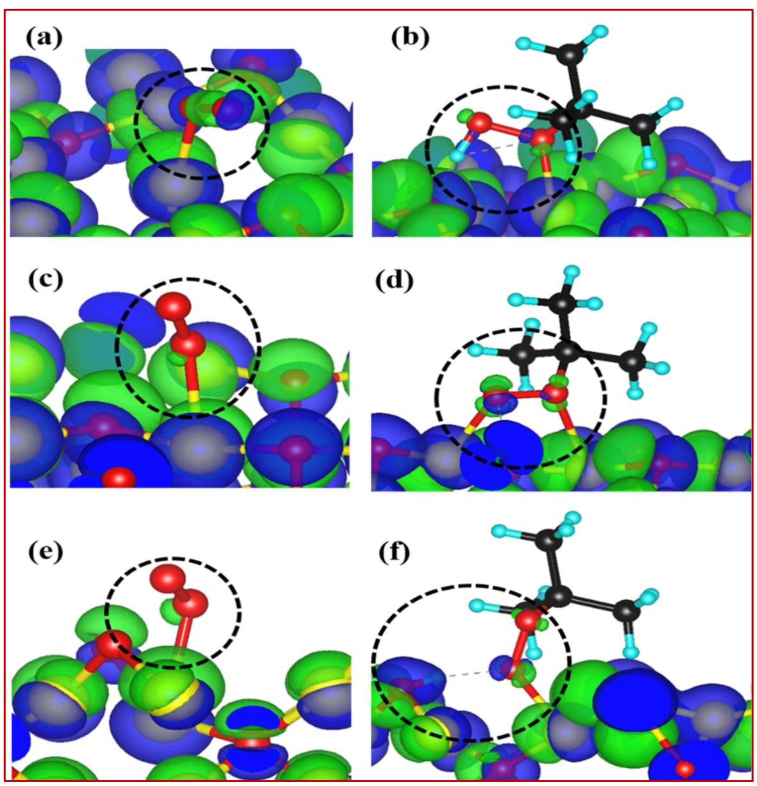

Fig. 3.20 The plots of charge density difference (CDD) of O_2 and t-butyl hydroperoxide (TBHP) adsorbed Cu_2O (111) (upper panel), Cu_2O (110) (middle panel), and Cu_2O (100)

(bottom panel) surfaces. Blue and light green regions in CDD represent charge depletion and accumulation, respectively. The iso-surface value is set from ± 0.025 to ± 0.06 e/Å^3 for CDD depending on the system. Color key: Cu (yellow), O (red), C (black), and H (cyan).

The Löwdin charge analysis shows that a net charge is transferred from (111) surface to the O_2 and TBHP molecules. A detailed analysis of the Löwdin charge analysis indicates that (111) surface loses electron density up to 0.3 e and 0.09 e in the case of O_2 and TBHP molecules, respectively. Contrary to this case, (110) surface gain electron density up to 0.03 e and 0.36 e in the case of O_2 and TBHP molecule, respectively. Similar to the case of (110) surface, (100) surface also gains electron density up to 0.12 e and 0.38 e for the O_2 and TBHP molecules, respectively. To picture the interaction among the different facets of Cu_2O with O_2 and TBHP molecules, the charge density difference (CDDs) of the combined systems were examined using Eq. 4 (in the experimental section) and presented in Fig. 3.20 These plots display the occurrence of the interaction at the interface among the surfaces with adsorbed O_2 and TBHP molecules. In the case of adsorption of only the O_2 molecule, the pronounced interaction observed over the (111) surface as compared to other facets of the Cu_2O is in line with the examined adsorption energy tabulated in Table 3.9 In the case of adsorption of the TBHP molecule, the oxygen atoms of the molecular framework of TBHP cause a pronounced interaction between the substrate and molecule for all the facets. It can be seen from Fig. 3.20 that the splitting of the H atom causes a strong interaction between the residual peroxide and surfaces resulting in higher adsorption energy for (100) surfaces. These findings are in agreement with the trend obtained for calculated adsorption energy.

Now, there is a question about how *c*-Cu_2O is much more active than the other shapes under the prevailing conditions. We observed that the mechanism through which the reaction proceeds matters. Also, the reaction parameters like polarity of the solvent system adopted, presence /absence of light, as well as the energetics of the reaction, play a very important role. It can be observed that the given chemical reaction proceeds through free radicals-based pathways where a cascade of the chemical events with electron transfer is very important. The solvent system which can stabilize the surface generated free radicals and drive them to take part in the subsequent chemical event should be the best. These directly affect the band-gap of the material. The E_g derived from the UV-Vis spectroscopy in MeCN (Fig. 3.12B), and in turn, Tauc plots of the solutions of all the NCs (Fig. 3.12 C) reveals that *o*-Cu_2O NCs have the minimum band-gap while the highest for *d*-Cu_2O and intermediate for *c*-Cu_2O. From the experimental results (Table 3.4), it can be observed that *c*-Cu_2O

is more catalytically active and completes the reaction in 3 days without catalyst annihilation while those of *d*-Cu_2O and *o*-Cu_2O are less active. Looking at the computational results of the optimized (100), (110), and (111) surfaces, it can be observed that the O-Cu bond length at the top layer is 1.80, 1.83, and 1.86 Å for *c*-Cu_2O, *d*-Cu_2O, and *o*-Cu_2O, respectively. In the case of *c*-Cu_2O, surface Cu atoms are more tightly bound with the surrounding O atoms compared to other surfaces. Hence, the weakly bonded Cu, in the case of (111) surfaces, easily leaches out from the surface to the solution in the form of Cu^{2+} ions. Also, (111) surfaces undergo reconstruction on binding with ROS species generated during the chemical reaction. This leaching/surface reconstruction deactivates the catalyst surface resulting in the saturation equilibrium state for a given chemical reaction. With (111) surfaces, the saturation equilibrium for the benzylic sp^3 C-H bond oxidation reached around 90% yield with the complete obliteration of the catalyst on the sixth day. However, in the case of (100) surfaces, the Cu atoms in a second layer bind tightly with the surrounding surface O atoms could not be in direct contact with any adsorbate, in turn, remain intact. The chemical kinetics and electrochemical analysis suggest Mars van- Krevalen type mechanism for the semiconductor metal oxides in the case of *c*-Cu_2O NCs (Scheme 3.4)[42,43].

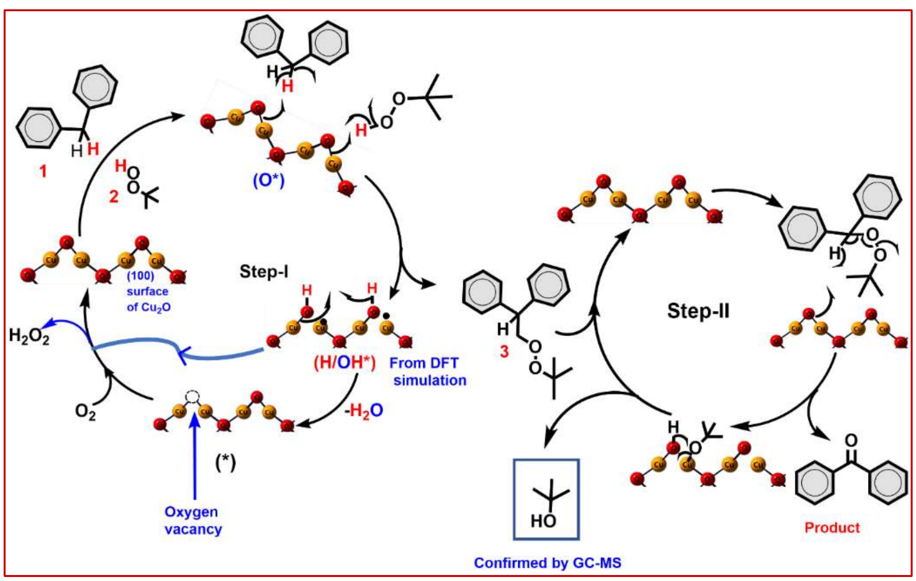

Scheme 3.4 Proposed reaction mechanism of benzylic sp^3 C−H bond oxidation of DPM with TBHP in the presence of *c*-Cu_2O NCs in the aerial atmosphere.

It can be observed from Scheme 1 that DPM (1) gets adsorbed through H-bonding with oxygen of Cu_2O (100) surface, in turn, TBHP is also chemisorbed in the vicinity on the surface, resulting in the cascade of the chemical events. Firstly, (100) surface lattice O-atoms (O^*) abstract H-atoms from the DPM and TBHP resulting in peroxo intermediate 3 which takes part in the second catalytic cycle leading to the product. These initial events generate two-electron reduced centers consisting of vicinal hydroxyl groups (H/OH^*), which in turn, generates oxygen vacancies (*) on the surface by ejecting the water molecule. Now, the reoxidation process of this oxygen vacancy is fast and an issue of debate. The reoxidation by O_2 molecule involves the following events: (1) activation of O_2 molecule by (*) resulting superoxo species (2) breaking of O-O bond resulting (100) surface lattice (O*) and one O atom (3) hopping of the O atom via lattice diffusion to refill another reduced center or oxidize the other species in the vicinity. The detailed study is out of the scope of this work. But, we can propose that the O atom may oxidize the water molecule into H_2O_2 again decompose into two water molecules in the catalytic loop and complete the cycle (Scheme 3.3)[43]. We recycled the c-Cu_2O for three consecutive cycles without affecting the % yield of the reaction (Fig. 3.21).

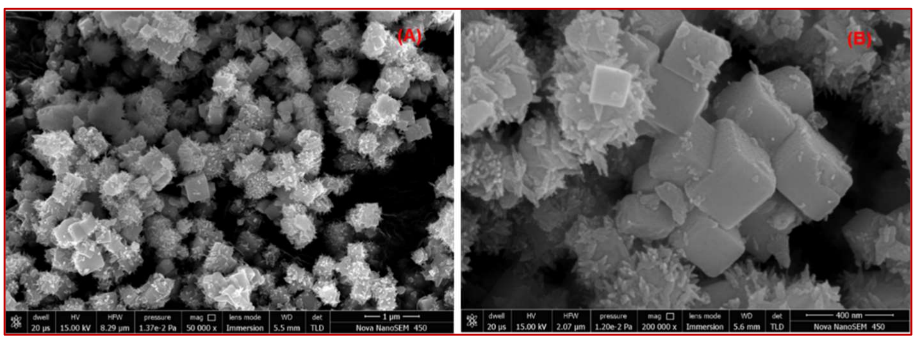

Fig. 3.21 FESEM images of recovered *c*-Cu_2O NCs at the end of third model reaction cycle.

On seeing the reaction mechanism, it is established that Cu_2O NCs can activate aerial oxygen molecule to the superoxo radical in turn, convert into hydroperoxo radical. This radical can be inserted into the 3˚ C-H bond of cumene resulting in industrially important CHP as a product. To demonstrate the applicability of the developed protocol, oxidation of cumene to CHP was carried out at RT by maintaining all the optimized reaction parameters (Scheme 3.5). We obtained a 95% yield with 70% selectivity for CHP as per confirmation from NMR spectroscopy and LC-MS analysis.

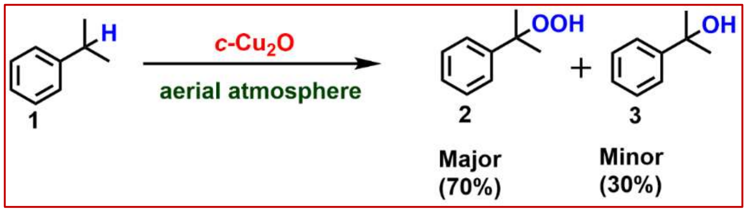

Scheme 3.5 Oxidation of Cumene to CHP with the developed protocol.

From the literature survey, it is observed that most of the facets of Cu_2O NCs are explored for the photocatalytic degradation of surface adsorbed dye molecules. For this purpose, it was proposed that the surface free electrons of various facets transfer from a surface to a pre-adsorbed substrate. Now, the facets with less band-bending can easily transfer the electrons/holes resulting in the degradation of the dye molecules due to a cascade of events beginning from the oxidation or reduction or both redox events[44–46.] However, in free radical-mediated organic transformations "the cascade" of chemical transformations is initiated due to ROSs responsible for end products. Recently, Wang et al demonstrated a new strategy to overcome the overoxidation in heterogeneous TiO_2 photocatalysis leading to photosynthesis. They showed that TiO_2 photocatalysis can integrate C–C and C═O formation in a tandem manner to achieve efficient oxidative cyclization for the syntheses of aryltetralones. They demonstrated that in contrast to conventional overoxidation, the radical cations possess sufficient reactivity toward nucleophilic addition, and single-electron transfer processes in TiO_2 photocatalysis can be developed into a powerful tool to construct C–C bonds and even strained carbon rings[47]. Now, in the case of copper-ended (111) surfaces, aerial oxygen molecule gets activated through SET from the surface copper ion forming end-on, η^1-superoxo radical, in turn, abstract •H radical from the peroxide intermediate (3) resulting in the product. This process left η^1-hydroperoxo species on the surface to convert to strongly oxidizing η^2-peroxo species responsible for lattice restructuring to CuO.[23] While in the case of oxygen-ended (100) surfaces, Mars van-Krevalen mechanism is dominated as discussed above. Here, the O_2 molecule is activated by vacancies created on the surface and not by SET processes. Hence, band-bending and charge-transfer concepts are not applicable here. Surface vacancies are refilled, here, by proton-coupled two electrons transfer process, regenerating the (100) surface ready for the next cycle. Hence, we recommend through this study that photochemical processes taking on the surface of semiconducting material should be differentiated into two categories: first band-gap dominant processes involving charge transfer through less band-bending of thin surface molecular layer leading to degradation or surface reconstruction mechanism and second, surface vacancies dominant processes involving charge transfer (mostly electrons) through the reduced center (*) leading to surface regeneration and stable chemical product.[48–50] Now addressing the question raised at the beginning of this study. It can be claimed that oxygen-ended *c*-Cu_2O (100) surfaces are inactive for photophysical and photochemical processes like dye degradation. But these {100} surface planes are highly active for metal oxide semiconductor-based oxidation processes (thorough Mars van-Krevelan catalytic cycles). These observations will be highly useful for the development of cheap and sustainable industrial oxidation processes.

3.6 Conclusions

(100), (111), and (110) faceted Cu_2O NCs having Cc, Oh, and Dh morphologies, respectively have been synthesized and characterized. The exposed facets of Cu_2O NCs were explored as catalytic sites for the benzylic sp^3C-H bond oxidation process under the optimized reaction conditions from the previous work. Based on experimental observations, chemical kinetics, electrochemical analyses and DFT studies, following conclusion can be drawn for the oxidation of benzylic C-H bond of DPM as a model reaction: (1) oxygen ended (100) facets of cubic Cu_2O NCs can do the oxidation process faster than any other facets within three days at RT with almost 100% yield and selectivity for the carbonyl product (2) Mars van-Krevalen mechanism is seem to be applicable for the oxidation processes on the (100) facets (3) the surface end oxygen atoms first abstract the ·H from the DPM and TBHP, forming the hydroperoxide take part in the second catalytic cycle for the product generation, leaving the oxygen vacancies/reduced center on the metal oxide surface (4) the resulting reduced center activate the aerial oxygen molecule to refill the vacancies and regenerate the catalytic surface (5) in case of Cu^{1+} ended (111) facets of *o*-Cu_2O NCs are capable to activate oxygen molecules to undergo reduction by SET mechanism in presence of light, and the in situ generated superoxo species immediately abstract the $^{\cdot}$H radical from the nearby substrate and initiate the cascade of chemical reactions and electronic processes resulting into stable oxidation product and complete restructuring of the crystal lattice of the catalyst, respectively (6) (100) surfaces of *c*-Cu_2O NCs seems to be activated for the processes where surface generated excitons transfer through band-gap are not required resulting into the desired oxidation product instead of complete degradation of the substrate and these processes become predominant when TBHP like mild oxidant (which can produce ·O-Bu^t like stable free radicals) present in the vicinity. Exciting results were obtained for the oxidation of compounds with multiple benzylic sp^3 C-H bonds on the (100)/(111) facets of the as-synthesized Cu_2O NCs which will be reported in a separate study.

Oxidation of Diphenylmethane. Diphenylmethane (0.166 mL, 1.0 mmol) was dissolved in 6.0 mL of acetonitrile in a 10 mL round-bottom flask and stirred for 5 min. o- Cu_2O NCs (3.5 mol%) were subsequently added, and the mixture was stirred for 10 min. Finally, 0.52 mL of t-butyl hydroperoxide (TBHP, 4.0 mmol) was added and the reaction mixture was stirred for 3 to 6 days at RT. The reaction progress was monitored on the TLC plate. After completing the reaction, the reaction mixture was centrifuged to recover the catalyst; the excess TBHP was destroyed by adding excess sodium metabisulfite into the reaction mixture. The excess reagents were distilled out. The product was extracted with ethyl acetate and dried over sodium sulfate. The crude product was purified by column chromatography using petroleum ether (60−80 °C) as an eluent. The product obtained was analyzed by ^1H NMR (Fig. 3.22 and 3.23).

Diphenylmethanone. White crystal; mp 47−49 °C. ^1H NMR ($CDCl_3$, 400 MHz): δ 7.84−7.81 (m, 4H), 7.61−7.59 (m, 2H), 7.52−7.28 (m, 4H). ^{13}C NMR ($CDCl_3$, 100 MHz) δ (ppm): 194.8, 137.5, 132.4, 130.1, 128.3. Purified by column chromatography on silica gel−10% EtOAc in petroleum ether as a mobile phase.

Oxidation of Cumene. 2.0 mmol of cumene and 3.5% *c*-Cu_2O NCs were mixed in a 10 mL round bottom flask without any solvent. The mixture was stirred at room temperature for three days under normal laboratory conditions. The reaction progress was monitored on the TLC plate. At the end of the third day the reaction mixture was analyzed directly without any purification by ^1H-NMR (Fig. 3.24), GC-MS (Fig.3.25 and Fig.3.26), and FTIR (Fig. 3.27 and Fig. 3.28) spectroscopies.

(2-hydroperoxypropan-2-yl) benzene (Cumene hydroperoxide). ^1H NMR ($CDCl_3$, 400 MHz): δ 7.53−7.51 (dd, 2H), δ 7.38-7.30 (t, 1H), δ 7.28-7.21 (t, 1H), δ 1.59 (s, 6H).

2-phenylpropan-2-ol (Cumyl alcohol). ^1H NMR ($CDCl_3$, 400 MHz): δ 7.53−7.40 (dd, 2H), δ 7.38-7.30(t, 1H), δ 7.28-7.21 (t, 1H), δ 1.61 (s, 6H).

Kinetic study of oxidation reactions

The reaction kinetics were studied by UV-Visible spectroscopy. To gain a deeper understanding of which facet is more efficient among all for a given desired product, a detailed kinetic experiment was carried out keeping in mind the effect of each facet on the rate of reaction. Eq. 2 shows a relation between the concentration of reactant and time.[34]

$$kt = \frac{1}{b-a} ln \frac{a(b-x)}{b(a-x)} \qquad (2)$$

where 'a' is the initial concentration of **1**, 'b' is the concentration of TBHP and 'x' is the concentration at time t. A plot of $\frac{1}{b-a} ln \frac{a(b-x)}{b(a-x)}$ versus time shows a straight line (figure S6) indicating that the reaction is first order with respect to DPM. The concentration of DPM was varied in the ratio of 24, 48, 72, 96, 120 with respect to catalyst amount (in mM), while the concentration of TBHP was kept constant.

Initial rates were determined for each mol of a substrate after the completion of the reaction (after 5 days) by monitoring the concentration of the product (benzophenone) by the UV spectral analysis. The kinetic experiment reveals that initial rates exhibited a linear dependence on [DPM] and first order with respect to the [DPM].

The Arrhenius equation (E_a = -slope*R, Where R is the universal gas constant i.e 8.314 J/mol and the temperature of the model reaction was set to 30°, 40°, 50°) was used to calculate the activation energy for all the morphologies of the catalyst at reaction temperature (Fig. 6C).

DFT Simulation. All DFT + U calculations were performed with the Quantum ESPRESSO codes.[51,52]The Perdew–Burke–Ernzerhof PBE functional was used with Grimme's D3(BJ) dispersion.[53]Based on our previous work [23] a U-j value of 6 eV was chosen for the Hubbard (+U) Cu d-state corrections. Standard PBE PAW (projector augmented wave) potentials were employed to represent the cores, whereas the valence electrons (Cu: $3d^{10}4s^1$, O: $2s^22p^4$, C: $2s^22p^2$, and H: $1s^1$) were treated by a plane-wave basis set with a 60 Ry kinetic energy cut-off.[57] The 4 × 2 and 3 × 2 supercells of 110 (Cu- and O-terminated) and 100 (O-terminated) facets of Cu_2O were modeled as periodic slabs which comprised seven atomic layers with a vacuum distance of 15 Å in the z-direction to avoid the interaction between the periodic images. The top four atomic layers were allowed to relax in all directions while others were kept fixed. A 5 × 4 × 1 and 5 × 8 × 1 Monkhorst–Pack k-point sampling grid were used for the Brillouin zone integration along with Marzari–

Vanderbilt cold smearing of 0.01 Ry and 0.03 Ry for Cu_2O (110) and Cu_2O (100) surfaces respectively throughout the calculations.[54,55] The geometry optimization was carried out until the residual force on each atom was smaller than 10^{-3} Ry/Bohr. To measure the strength of the interaction between the adsorbent and the substrate, the adsorption energy (E_{ads}) calculated using the following formula,

$$E_{ads} = E_{(substrate+adsorbent)} - E_{(substrate)} - E_{(adsorbent)} \quad (3)$$

Where, $E_{(substrate+adsorbent)}$ is the total energy of the adsorbed system. $E_{(substrate)}$ and $E_{(adsorbent)}$ are the total energies of the clean surface and molecule in the gas phase, respectively. The charge density difference of systems was plotted as,

$$\Delta\rho(r) = \rho(r)_{(substrate+adsorbent)} - \rho(r)_{(substrate)} - \rho(r)_{(adsorbent)} \quad (4)$$

Where, $\rho(r)_{(substrate+adsorbent)}$, $\rho(r)_{(substrate)}$, and $\rho(r)_{(adsorbent)}$ are the charge densities distribution on the substrate + adsorbent, pristine substrate, and isolated adsorbent systems, respectively.

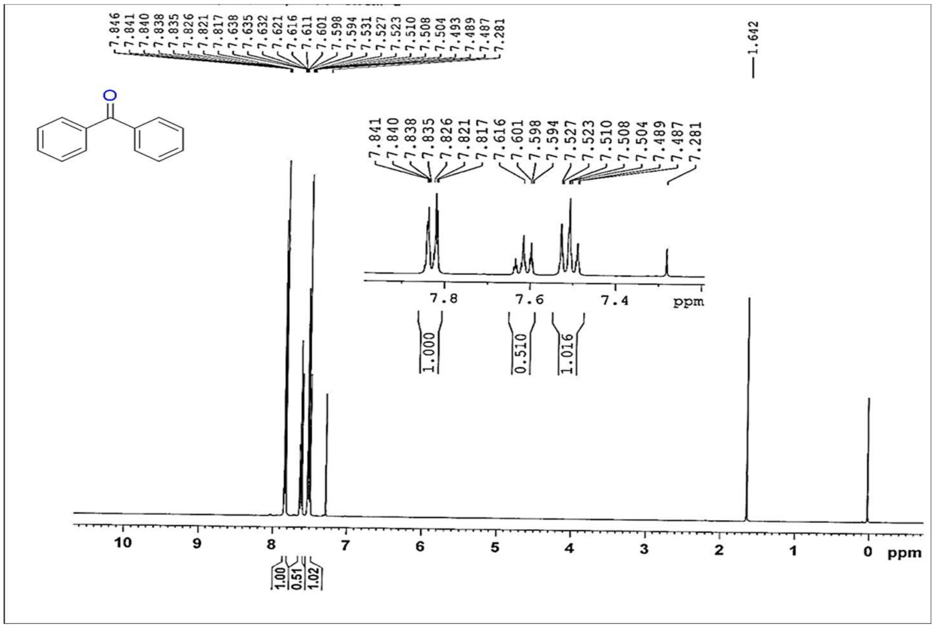

Fig. 3.22 ^{1}H NMR of Diphenylmethanone (benzophenone).

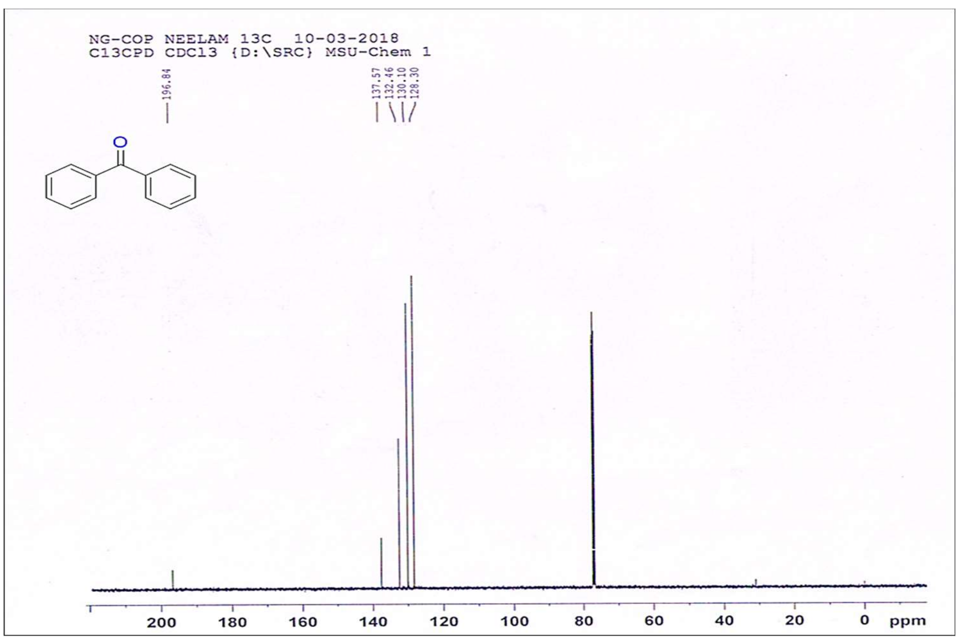

Fig. 3.23 ^{13}C NMR of Diphenylmethanone (benzophenone).

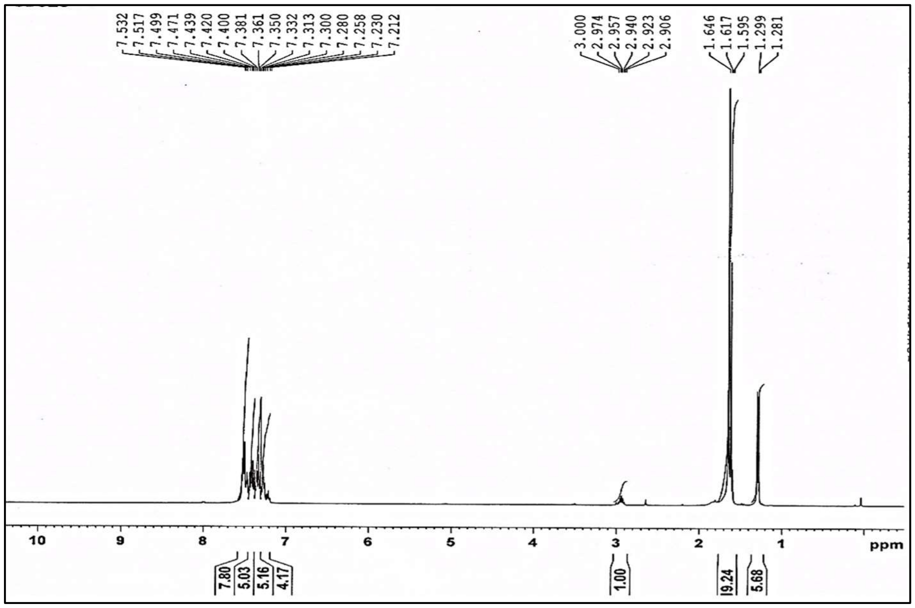

Fig. 3.24 ^{1}H NMR of the reaction mixture of oxidation of cumene in presence of *c*-Cu_2O NCs at the end of 3rd day showing the presence of cumene hydroperoxide as a major and cumyl alcohol as a minor product.

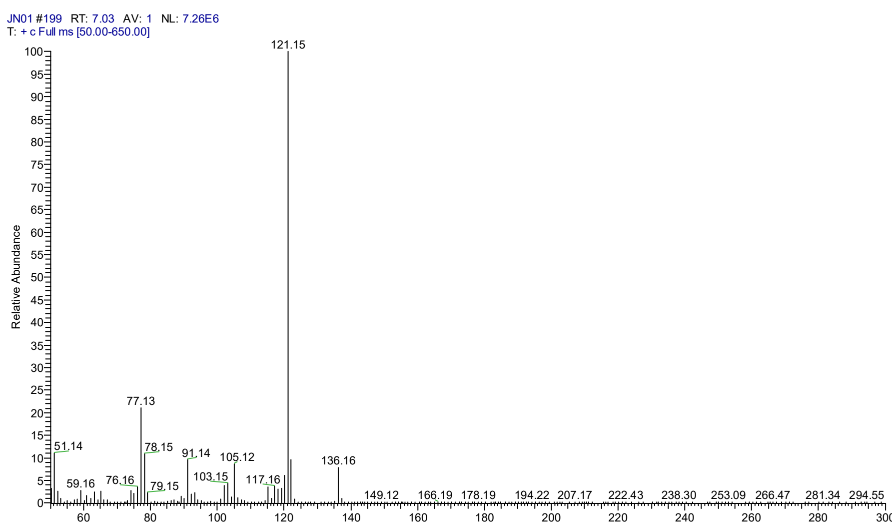

Fig. 3.25 GC-MS of the reaction mixture of oxidation of cumene in presence of *c*-Cu_2O NCs at the end of 3rd day showing the cumyl alcohol as a minor product.

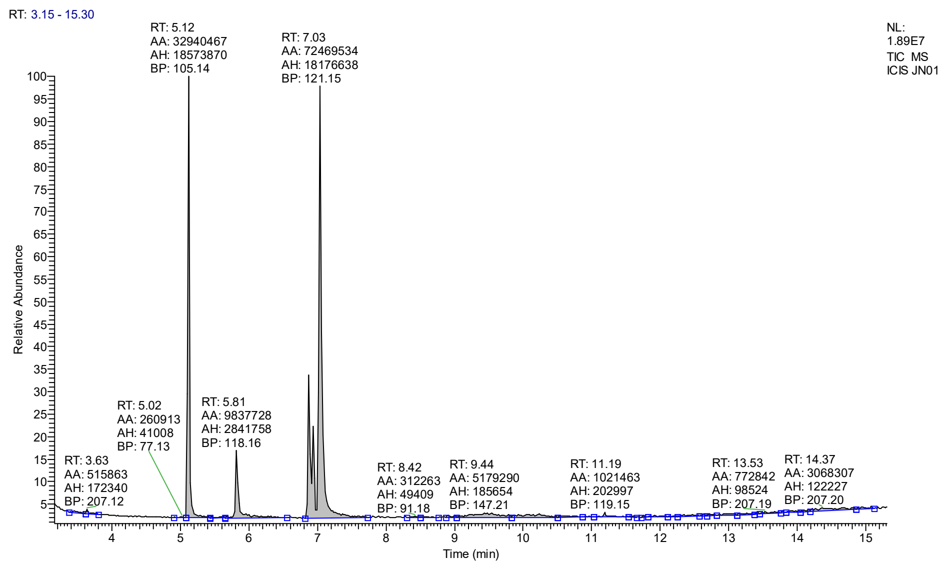

Fig. 3.26 GC-MS of the reaction mixture of oxidation of cumene in presence of *c*-Cu_2O NCs at the end of 3rd day showing the presence of cumyl alcohol as a minor product.

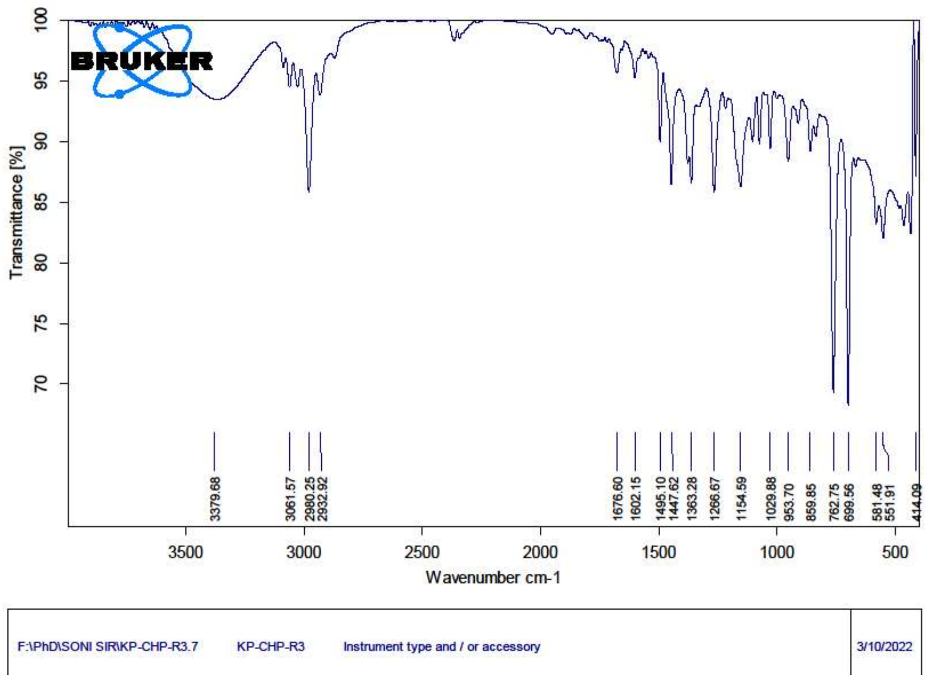

Fig.3.28 FTIR Spectra of the reaction mixture of oxidation of cumene in presence of *c*-Cu_2O NCs at the end of 3rd day showing the presence of cumene hydroperoxide and cumyl alcohol. (Neat without KBr)

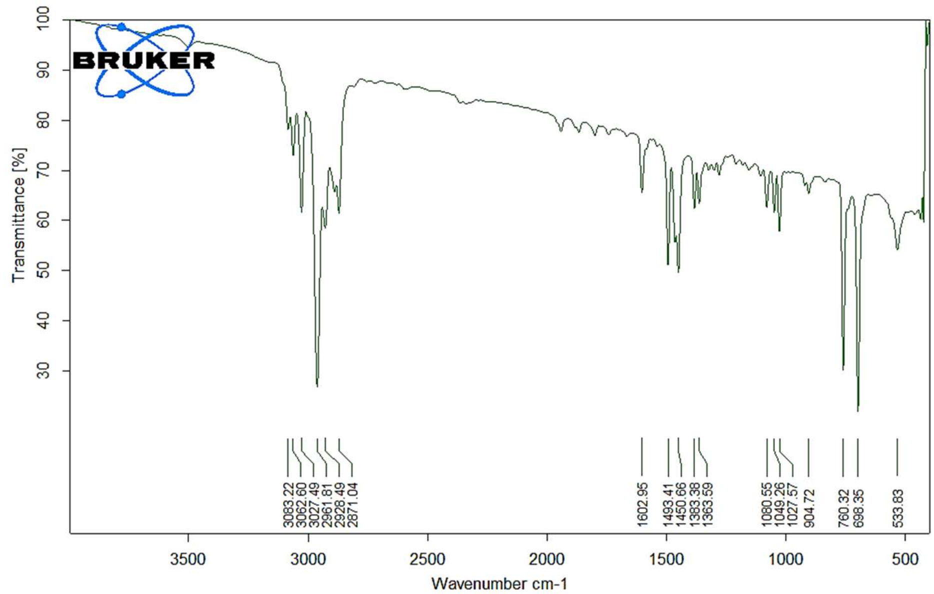

Fig. 3.28. FTIR Spectra of Cumene (Reactant only) (Neat without KBr)

3.7 References

(1) Zhou, K.; Wang, X.; Sun, X.; Peng, Q.; Li, Y. Enhanced Catalytic Activity of Ceria Nanorods from Well-Defined Reactive Crystal Planes. *J. Catal.* **2005**, *229*, 206–212.

(2) Tan, C.-S.; Hsu, S.-C.; Ke, W.-H.; Chen, L.-J.; H. Huang, M. Facet-Dependent Electrical Conductivity Properties of Cu_2O Crystals. *Nano Lett.* **2015**, *15*, 2155–2160.

(3) H. Huang, M.; Naresh, G.; Chen, H.-S. Facet-Dependent Electrical, Photocatalytic, and Optical Properties of Semiconductor Crystals and Their Implications for Applications. ACS Appl. Mater. Interfaces **2017**, *10*, 4–15.

(4) Huang, W.-C.; Lyu, L.-M.; Yang, Y.-C.; H. Huang, M. Synthesis of Cu_2O Nanocrystals from Cubic to Rhombic Dodecahedral Structures and Their Comparative Photocatalytic Activity. *J. Am. Chem. Soc.* **2011**, *134*, 1261–1267.

(5) Shang, Y.; Guo, L. Facet-Controlled Synthetic Strategy of Cu_2O-Based Crystals for Catalysis and Sensing. *Adv. Sci.* **2015**, *2*, 1500140.

(6) Bai, S.; Wang, L.; Li, Z.; Xiong, Y. Facet-Engineered Surface and Interface Design of Photocatalytic Materials. *Adv. Sci.* **2017**, *4*, 1600216.

(7) Hua, Q.; Cao, T.; Bao, H.; Jiang, Z.; Huang, W. Crystal-Plane-Controlled Surface Chemistry and Catalytic Performance of Surfactant-Free Cu_2O Nanocrystals. *ChemSusChem* **2013**, *6*, 1966–1972.

(8) Ho, J. Y.; Huang, M. H. Synthesis of Submicrometer-Sized Cu_2O Crystals with Morphological Evolution from Cubic to Hexapod Structures and Their Comparative Photocatalytic Activity. *J. Phys. Chem. C* **2009**, *113*, 14159–14164.

(9) Tsai, Y. H.; Chanda, K.; Chu, Y. T.; Chiu, C. Y.; Huang, M. H. Direct Formation of Small Cu_2O Nanocubes, Octahedra, and Octapods for Efficient Synthesis of Triazoles. *Nanoscale* **2014**, *6*, 8704–8709.

(10) Chanda, K.; Rej, S.; Huang, M. H. Investigation of Facet Effects on the Catalytic Activity of Cu_2O Nanocrystals for Efficient Regioselective Synthesis of 3,5-Disubstituted Isoxazoles. *Nanoscale* **2013**, *5*, 12494–12501.

(11) Xu, Y.; Wang, H.; Yu, Y.; Tian, L.; Zhao, W.; Zhang, B. Cu_2O Nanocrystals: Surfactant-Free Room-Temperature Morphology-Modulated Synthesis and Shape-Dependent Heterogeneous Organic Catalytic Activities. *J. Phy. Chem. C* **2011**, *115*, 15288–15296.

(12) Li, M.; Xing, X.; Ma, Z.; Lv, J.; Fu, P.; Li, Z. Synthesis of Composition Tunable and (111)-Faceted Cu/Cu_2O Nanoparticles toward Photocatalytic, Ligand-Free, and Solvent-Free C–N Ullmann Coupling Reactions. *ACS Sustain. Chem. Eng* **2018**, *6*, 5495–5503.

(13) Sheldon, R. A.; Bekkum, Ed. van H. *Fine Chemicals through Heterogeneous Catalysis, Wiley-VCH: Verlag CimbH, 2001.***1992**, 24.

(14) Stalh. S. S,; P. L. Ed., Alsters. *Liquid Phase Aerobic Oxidation Catalysis: Industrial Applications and Academic Perspectives, Wiley-VCH, Weinheim,* **2016**, 2546.

(15) Karimov, R. R.; Hartwig, J. F. Transition-Metal-Catalyzed Selective Functionalization of C(Sp^3)−H Bonds in Natural Products. *Angew. Chem. Int. Ed.* **2018**, *57*, 4234–4241.

(16) De Houwer, J.; Abbaspour Tehrani, K.; Maes, B. U. W. Synthesis of Aryl(Di)Azinyl Ketones through Copper- and Iron-Catalyzed Oxidation of the Methylene Group of Aryl(Di)Azinylmethanes. *Angew. Chem. Int. Ed.* **2012**, *51*, 2745–2748.

(17) Recupero, F.; Punta, C. Free Radical Functionalization of Organic Compounds Catalyzed by N-Hydroxyphthalimide. *Chem. Rev.* **2007**, *107*, 3800–3842.

(18) Bohinski, T.; Ryan, T. P.; Abduh, N. A. Y.; Al-garni, T.; Kahtani, A. Al; Aouissi, A. Selective Oxidation of Cumene into 2-Phenyl-2- Propanol and Acetophenone over Activated Carbon Supported $Co_{1.5}PW_{12}O_{40}$ material. *Mater. Res. Express* **2020**, 7, 025606.

(19) Chang, Y.; Xiulong, S.; Zhi, D. Z.; Liu,Y. Preparation and Catalysis of Chloromethylated Polystyrene-Supported Macrocyclic Schiff Base Metal Complexes for the Oxidation of Cumene. *Polym. Adv. Technol.* **2008**, 19, 877–881.

(20) Hara, T.; Iwahama, T.; Sakaguchi, S.; Ishii, Y. Catalytic Oxyalkylation of Alkenes with Alkanes and Molecular Oxygen via a Radical Process Using N-Hydroxyphthalimide. *The J. Org. Chem.* **2001**, *66*, 6425–6431.

(21) Fukuda, O.; Sakaguchi, S.; Ishii, Y. Preparation of Hydroperoxides by N-Hydroxyphthalimide-Catalyzed Aerobic Oxidation of Alkylbenzenes and Hydroaromatic Compounds and Its Application. *Adv. Synth. Catal.* **2001**, *343*, 809–813.

(22) Lu, Q.; Shi, G.; Zhou, H.; Yuan, E.; Chen, C.; Ji, L. A Highly Efficient Transformation from Cumene to Cumyl Hydroperoxide via Catalytic Aerobic Oxidation at Room Temperature and Investigations into Solvent Effects, Reaction Networks and Mechanisms. *Appl. Catal. A: Gen.* **2022**, *630,* 118441.

(23) Gupta, N.; Machhi, H. K.; A. Baraiya, B.; S. Soni, S.; V. Bedekar, A.; K. Jha, P.; P. Soni, H. Benzylic Csp^3–H Bond Oxidation on the (111) Facets of Octahedral Cu_2O Nanocrystals. *ACS Appl. Nano Mater.* **2021**, *4*, 7840–7855.

(24) Machhi, H.K.; K. Sonigara, K.; N. Bariya, S.; P. Soni, H.; S. Soni, S. Hierarchically Porous Metal–Organic Gel Hosting Catholyte for Limiting Iodine Diffusion and Self-Discharge Control in Sustainable Aqueous Zinc–I_2 Batteries. *ACS Appl. Mater. Interfaces* **2021**, *13*, 21426–21435.

(25) Pal, J.; Ganguly, M.; Mondal, C.; Roy, A.; Negishi, Y.; Pal, T. Crystal-Plane-Dependent Etching of Cuprous Oxide Nanoparticles of Varied Shapes and Their Application in Visible Light Photocatalysis. *J. Phys. Chem. C* **2013**, *117*, 24640–24653.

(26) Jenkins R.; Synder, R. L. Introduction to X-ray powder diffractometry. *John Wiley and Sons, New York 1996* **2011**, *11*, 277–278.

(27) Sahai, A.; Goswami, N.; Kaushik, S. D.; Tripathi, S. Cu/Cu_2O/CuO Nanoparticles: Novel Synthesis by Exploding Wire Technique and Extensive Characterization. *Appl. Surf. Sci.* **2016**, *390*, 974–983.

(28) Mote, V.; Purushotham, Y.; Dole, B. Williamson-Hall Analysis in Estimation of Lattice Strain in Nanometer-Sized ZnO Particles. *J. Theor. Appl. Phys.* **2012**, *6*, 2–9.

(29) Bai, Y.; Yang, T.; Gu, Q.; Cheng, G.; Zheng, R. Shape Control Mechanism of Cuprous Oxide Nanoparticles in Aqueous Colloidal Solutions. *Powder Technol.* **2012**, *227*, 35–42.

(30) Crnjak Orel, Z.; Anžlovar, A.; Dražić, G.; Žigon, M. Cuprous Oxide Nanowires Prepared by an Additive-Free Polyol Process. *Cryst. Growth Des.* **2007**, *7*, 453–458.

(31) Chu, C. Y.; Huang, M. H. Facet-Dependent Photocatalytic Properties of Cu_2O Crystals Probed by Using Electron, Hole and Radical Scavengers. *J. Mater. Chem. A* **2017**, *5*, 15116–15123.

(32) Chen, T.-N.; Kao, J.-C.; Zhong, X.-Y.; Chan, S.-J.; S. Patra, A.; Lo, Y.-C.; H. Huang, M. Facet-Specific Photocatalytic Activity Enhancement of Cu_2O Polyhedra Functionalized with 4-Ethynylanaline Resulting from Band Structure Tuning. *ACS Cent. Sci.* **2020**, *6*, 984–994.

(33) Su, Y.; Li, H.; Ma, H.; Robertson, J.; Nathan, A. Controlling Surface Termination and Facet Orientation in Cu_2O Nanoparticles for High Photocatalytic Activity: A Combined Experimental and Density Functional Theory Study. *ACS Appl. Mater. Interfaces* **2017**, *9*, 8100–8106.

(34) Liang, Y.; Yi, C.; Tricard, S.; Fang, J.; Zhao, J.; Shen, W. Prussian Blue Analogues as Heterogeneous Catalysts for Epoxidation of Styrene. *RSC Adv.* **2015**, *5*, 17993–17999.

(35) Zhang, Z.; Wang, S. S.; Song, R.; Cao, T.; Luo, L.; Chen, X.; Gao, Y.; Lu, J.; Li, W. X.; Huang, W. The Most Active Cu Facet for Low-Temperature Water Gas Shift Reaction. *Nat. Commun.* **2017**, *8*, 1–10.

(36) Sandford, C.; Edwards, M. A.; Klunder, K. J.; Hickey, D. P.; Li, M.; Barman, K.; Sigman, M. S.; White, H. S.; Minteer, S. D. A Synthetic Chemist's Guide to Electroanalytical Tools for Studying Reaction Mechanisms. *Chem. Sci.* **2019**, *10*, 6404–6422.

(37) Paliwal, M. K.; Meher, S. K. Study of "Ni-Doping" and "Open-Pore Microstructure" as Physico-Electrochemical Stimuli towards the Electrocatalytic Efficiency of Ni/NiO for the Oxygen Evolution Reaction. *New J. Chem.* **2020**, *44*, 17507–17517.

(38) Von Hauff, E. Impedance Spectroscopy for Emerging Photovoltaics. *J. Phys. Chem. C* **2019**, *123*, 11329–11346.

(39) Adams, R. N. Electrocbemistry at Solid ELectrds. **1969**, 1–27.

(40) Ning, J.; He, Q.; Luo, X.; Wang, M.; Liu, D.; Wang, J.; Liu, J.; Li, G. Rapid and Sensitive Determination of Vanillin Based on a Glassy Carbon Electrode Modified with Cu_2O-Electrochemically Reduced Graphene Oxide Nanocomposite Film. *Sensors* **2018**, *18*. 2762.

(41) Li, L.; Zhang, R.; Vinson, J.; L. Shirley, E.; P. Greeley, J.; R. Guest, J.; K. Y. Chan, M. Imaging Catalytic Activation of CO_2 on Cu_2O (110): A First-Principles Study. *Chem. Mater.* **2018**, *30*, 1912–1923.

(42) Isseroff Bendavid, L.; A. Carter, E. First-Principles Predictions of the Structure, Stability, and Photocatalytic Potential of Cu_2O Surfaces. *J. Phys. Chem. B* **2013**, *117*, 15750–15760.

(43) Soon, A.; Todorova, M.; Delley, B.; Stampfl, C. Thermodynamic Stability and Structure of Copper Oxide Surfaces : A First-Principles Investigation. Phys. Rev. B Condens. Matter **2007**, 76, 1–9.

(44) Deshlahra, P.; T. Carr, R.; Chai, S.-H.; Iglesia, E. Mechanistic Details and Reactivity Descriptors in Oxidation and Acid Catalysis of Methanol. *ACS Catal.* **2014**, *5*, 666–682.

(45) Chen, K.; Iglesia, E.; Bell, A. T. Isotopic Tracer Studies of Reaction Pathways for Propane Oxidative Dehydrogenation on Molybdenum Oxide Catalysts. *J. Phys. Chem. B* **2001**, *105*, 646–653.

(46) Kwon, S.; Deshlahra, P.; Iglesia, E. Dioxygen Activation Routes in Mars-van Krevelen Redox Cycles Catalyzed by Metal Oxides. *J. Catal.* **2018**, *364*, 228–247.

(47) Liu, Y.; Zhang, M.; Tung, C.-H.; Wang, Y. TiO_2 Photocatalytic Cyclization Reactions for the Syntheses of Aryltetralones. *ACS Catal.* **2016**, *6*, 8389–8394.

(48) Chen, Y.-J.; Chiang, Y.-W.; H. Huang, M. Synthesis of Diverse Ag_2O Crystals and Their Facet-Dependent Photocatalytic Activity Examination. *ACS Appl. Mater. Interfaces* **2016**, *8*, 19672–19679.

(49) Yuan, G. Z.; Hsia, C. F.; Lin, Z. W.; Chiang, C.; Chiang, Y. W.; Huang, M. H. Highly Facet-Dependent Photocatalytic Properties of Cu_2O Crystals Established through the Formation of Au-Decorated Cu_2O Heterostructures. *Chem. Eur. J.* **2016**, *22*, 12548–12556.

(50) Ma, B.; Kong, C.; Lv, J.; Zhang, W.; Guo, J.; Zhang, X.; Yang, Z.; Yang, S. Controllable In-Situ Synthesis of Cu–Cu2O Heterostructures with Enhanced Visible-Light Photocatalytic Activity. *ChemistrySelect* **2018**, *3* (38), 10641–10645. https://doi.org/10.1002/slct.201802880.

(51) Giannozzi, P.; Baroni, S.; Bonini, N.; Calandra, M.; Car, R.; Cavazzoni, C.; Ceresoli, D.; Chiarotti, G. L.; Cococcioni, M.; Dabo, I.; Dal Corso, A.; De Gironcoli, S.; Fabris, S.; Fratesi, G.; Gebauer, R.; Gerstmann, U.; Gougoussis, C.; Kokalj, A.; Lazzeri, M.; Martin-Samos, L.; Marzari, N.; Mauri, F.; Mazzarello, R.; Paolini, S.; Pasquarello, A.; Paulatto, L.; Sbraccia, C.; Scandolo, S.; Sclauzero, G.; Seitsonen, A. P.; Smogunov, A.; Umari, P.; Wentzcovitch, R. M. Quantum Espresso: A Modular and Open-Source Software Project for Quantum Simulations of Materials. *J. Phys. Condens. Matter* **2009**, *21,* 395502.

(52) Giannozzia, P.; Andreussib, O.; Brummec, i. T.; Brummec, O; Bunaud, M.; Buongiorno, N.; Calandrad, M.; Carf, R.; Cavazzonig, C.; Ceresolih, D.; M. C. et al. Advanced Capabilities for Materials Modelling with Quantum Espresso. *Mater. Res. Express* **2019**, 0–12.

(53) Stefan, Grimme; Stephan, Ehrlich; Stefan, L. G. Effect of the Damping Function in Dispersion Corrected Density Functional Theory. *J. Comput. Chem* **2012**, *32*, 174–182. https://doi.org/10.1002/jcc.

(54) Pack, H. J. M.; Hendrik, J . D. Special Points for Brillonin-Zone Integrations. *Physical Review* **2018**, *13*, 10–27.

(55) Marzari, N.; Vanderbilt, D.; De Vita, A.; Payne, M. C. Thermal Contraction and Disordering of the Al(110) Surface. *Phy. Rev. Lett.* **1999**, *82*, 3296–3299.

This work has been published in Journal of Molecular Catalysis.

https://doi.org/10.1016/j.mcat.2022.112490

Molecular Catalysis 528 (2022) 112490

ELSEVIER

Contents lists available at ScienceDirect

Molecular Catalysis

journal homepage: www.journals.elsevier.com/molecular-catalysis

Check for updates

Differentiating the {100} surfaces of Cu_2O nanocrystals from {111} and {110} for benzylic C_{sp}3-H bond oxidation: Oxidations of diphenyl methane to benzophenone and cumene to cumene hydroperoxide under mild conditions

Neelam Gupta [a], Bhumi A. Baraiya [b], Prafulla K. Jha [b], Hemant P. Soni [a,*]

[a] Department of Chemistry, Faculty of Science, The Maharaja Sayajirao University of Baroda, Vadodara, Gujarat 390002, India
[b] Department of Physics, Faculty of Science, The Maharaja Sayajirao University of Baroda, Vadodara, Gujarat 390002, India